Asymptotic analysis for late coda correlations under different geometric distributions of earthquakes

Yingjie Xia [1,2,3], Xuping Feng [1,2], and Xiaofei Chen [1,2]

[1]Shenzhen Key Laboratory of Deep Offshore Oil and Gas Exploration Technology, Southern University of Science and Technology, Shenzhen, China

[2]Department of Earth and Space Sciences, Southern University of Science and Technology, Shenzhen, China

[3]Department of Mechanics and Aerospace Engineering, Harbin Institute of Technology, Harbin, China

Key Points:

- The dimension of the stationary phase zone is inversely proportional to the newly-proposed k-κ coefficient
- Most of the large earthquakes situate in the stationary phase zone for constructing the inter-station wave in late coda correlations
- The event-receiver geometry can result in the emergence time variation up to 1/6 of the body wave correlation period

Corresponding author: Yingjie Xia, 11749314@mail.sustech.edu.cn

Abstract

Some features in late coda correlations have now been commonly treated as "the inter-station body waves". In general, however, large earthquakes releasing coda waves mostly situate at the continental boundaries. It remains unclear as to how such a discrete and non-uniform distribution of earthquakes influences these features. To understand the impacts, here we introduce geometric ray theory to explore the body wave cross-correlation. In the stationary phase integral, we show that the distribution geometry of earthquakes and the dimension of the stationary phase zone significantly influence the correlation phases. The dimension of the stationary phase zone is inversely proportional to the k-κ coefficient which, as a newly-proposed terminology, is composed of the seismic wave-number and the coda propagation distance. In late coda correlations, most of the large earthquakes situate in the stationary phase zone for constructing the inter-station wave due to the small k-κ coefficient. However, because earthquakes are not always at the stationary points, the correlation signals may appear a little earlier than their counterparts in Green's function. We have verified the theoretical analyses with the synthetic and realistic coda correlations. This theory is also applicable in other physics fields allowing for geometric ray theory. It demonstrates that the event-receiver geometry can result in the travel time variation up to 1/6 of the body wave correlation period. Thus, researchers should carefully investigate the impacts when utilizing the correlation signals as inter-station body waves for the future work of illuminating the Earth's discontinuities.

1 Introduction

With massive retrieval of surface waves in the noise correlation (e.g., Campillo & Paul, 2003; Shapiro & Campillo, 2004), body wave reflections have also been reported in the last over ten years (e.g., Roux et al., 2005; Tonegawa et al., 2009; Zhan et al., 2010; Lin et al., 2013). Recent developments have shown that after stacking the interferometric seismograms according to the inter-station distance bins, the noise correlation can produce signals like the Earth's deep reflections e.g. the ScS wave reflected from the core-mantle boundary (Lin et al., 2013). The application begins with the work of Poli et al. (2012) in retrieving the body waves reflections from the mantle transition zones. The later studies show that these reflections are mainly contributed by fruitful earthquake codas in seismic noise (Lin et al., 2013; Boué et al., 2014), partially because multiple reverberations of seismic body waves dissipate plenty of energy within the Earth, and only large earthquakes (approximate $\geq M7.0$) can release sufficiently powerful coda waves to produce such deep reflections. The late earthquake coda correlations (approximately 3−10 hours after the origin time of earthquakes) have produced a wealth of deep reflections (Pham et al., 2018; Li et al., 2020).

These waves provide dense ray path coverage at the discontinuities below seismic networks, thus allowing for complementary characterization of the deep layering properties (Poli et al., 2015; Huang et al., 2015; Tkalčić & Pham, 2018).

While one uses the travel times to carry out reliable travel time tomography, the reconstructed deep reflections must converge to the counterparts in Green's function of the propagation medium. The convenient relationship is likely true, for example, in a homogeneous medium with uniform distributions of noise sources (e.g., Snieder, 2004; Sánchez-Sesma & Campillo, 2006; Tanimoto, 2008; Tsai, 2009). It is also valid in an inhomogeneous medium when even and uncorrelated sources situate in an enclosed surface far from the stations (Wapenaar, 2004; Wapenaar & Fokkema, 2006). For the summary, readers can refer to (Boschi & Weemstra, 2015; Fichtner & Tsai, 2019). These theories substantially assume a uniform distribution of noise sources. However, the assumption is unsatisfied because large earthquakes radiating coda waves mostly locate at continental boundaries and the distribution is obviously non-uniform. Seismic coda waves are mainly made of strong reverberations in the great-circle plane constrained by the earthquake and station (Sens-Schönfelder et al., 2015). It is well known that the directionality and non-uniformity of noise sources affect phase variations of the inter-station surface waves (Tsai, 2009; Yao & van der Hilst, 2009; Froment et al., 2010; Tatiana et al., 2016). The non-uniform earthquake distribution may also result in the body wave correlation phase variations, which subsequently biases the travel time measurements of the reconstructed deep reflections resorting to the alignment of waveform peaks in practice.

Using sensitivity kernels for the noise correlation can precisely evaluate the correlation phases (Tromp et al., 2010). The approach is adapted to even complex scenarios including the source distributions, the medium structures, and the data preprocessing (Fichtner et al., 2016). Another numerical approach is to synthesize the interferometric seismograms in controlled circumstances, for instance, in the radially stratified earth model with preferable layouts of earthquakes and stations. Such numerical experiments provide us with intuitive knowledge of the phase variations caused by the effective duration of late codas and the event-receiver geometries (Sager et al., 2018; Wu et al., 2018; Wang & Tkalčić, 2020). For a thorough understanding, it is preferred to conduct a theoretical analysis. For example, Liu & Zhang (2018) have shown that for a laterally uniform distribution of noise sources, the travel times of interferometric SH body waves are the same as those in Green's function of the radially stratified earth model. Kennett & Pham (2018) have introduced the ray-theoretical framework to investigate the phase properties of seismic reflections and the spurious waves that extensively appear at the arrival time differences of the conventional deep reflections (Boué et al., 2014; Pham et al., 2018; Li et al., 2020). They show that the correlations of

coda waves with the same slowness contribute to the two types of features. To investigate the phase variations caused by the geometric distribution of earthquakes, we follow the way.

We establish the correlation theory for body waves in a smooth medium with discontinuities, comparable to the realistic large-scale earth structure. The geometric ray approximation only considers the first term in the series of the ray ansätze (Chapman, 2004, chapter 5.1). It provides an appropriate mathematical formula describing the propagation of teleseismic body waves in the study. In the second section, based on the stationary phase integral of the cross-correlation function (CCF), we show that the distribution geometry of earthquakes and the k-κ coefficient affect the correlation phases, and the k-κ coefficient decides the dimension of the stationary phase zone. In the third section, we use the k-κ coefficient to study the late coda correlations; we validate the theoretical analysis using synthetic and realistic coda correlations. Finally, we use the current theory to interpret Lobkis & Weaver (2001)'s ultrasonic laboratory test that primarily facilitates noise interferometry.

2 Theory

2.1 The Correlation of Body Waves

We study the cross-correlation of body waves in an inhomogeneous and isotropic medium, with the density $\rho(\boldsymbol{x})$, and the two Lamé moduli $\lambda(\boldsymbol{x})$ and $\mu(\boldsymbol{x})$. $\boldsymbol{x} = (x_1, x_2, x_3)$ represents a point in the medium. Hereafter we use boldface type to express a vector or matrix. As the medium is isotropic, body waves in the medium are in the form of P and S waves in geometric ray theory, with the velocity $\alpha(\boldsymbol{x}) = \sqrt{[\lambda(\boldsymbol{x}) + 2\mu(\boldsymbol{x})]/\rho(\boldsymbol{x})}$ and $\beta(\boldsymbol{x}) = \sqrt{\mu(\boldsymbol{x})/\rho(\boldsymbol{x})}$, respectively. There are two receivers at $\boldsymbol{x}_a$ and $\boldsymbol{x}_b$ at the surface. The noise sources accumulate in the region $V = V_- + V_+$, with the subscripts $-$ and $+$ designating at the negative and positive sides of two stations, respectively (Figure 1).

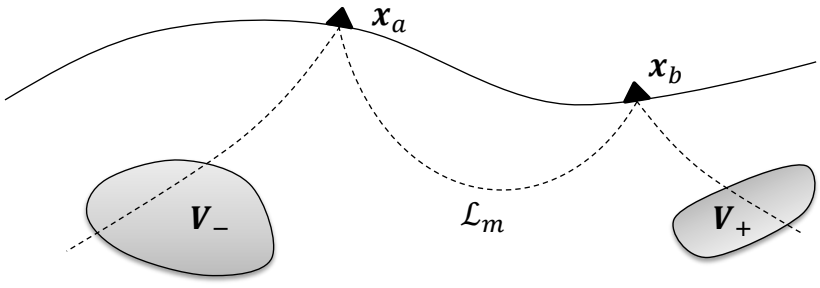

Figure 1. Body wave propagation in the medium. V_- and V_+ are noise source regions (gray) at the negative and positive sides of two stations $\boldsymbol{x}_a$ and $\boldsymbol{x}_b$ (triangles) on the medium surface. $\mathcal{L}_m$ is a ray passing through $\boldsymbol{x}_a$, $\boldsymbol{x}_b$ and the source region.

We assume the source region V is homogeneous and there are point sources in V with the source spectrum $N(\omega, \boldsymbol{x})$. For a continuous set of the source distribution, $N(\omega, \boldsymbol{x})$ is the source spectrum density, i.e., the source spectrum per unit volume. The body wave velocity records at a high angular frequency ω can be represented by the expansion of rays as (in chapter 5.3, Chapman, 2004)

$$\begin{aligned} u(\omega, \boldsymbol{x}, \boldsymbol{x}_a) =& N(\omega, \boldsymbol{x}) \sum_m f(\omega, \boldsymbol{x}, \boldsymbol{x}_a, \mathcal{L}_m) e^{i\omega T(\boldsymbol{x}, \boldsymbol{x}_a, \mathcal{L}_m)} \\ u(\omega, \boldsymbol{x}, \boldsymbol{x}_b) =& N(\omega, \boldsymbol{x}) \sum_n f(\omega, \boldsymbol{x}, \boldsymbol{x}_b, \mathcal{L}'_n) e^{i\omega T(\boldsymbol{x}, \boldsymbol{x}_b, \mathcal{L}'_n)} \end{aligned}, \tag{1}$$

with i denoting the imaginary unit, and the ray descriptors $\mathcal{L}_m(\boldsymbol{x})$ and $\mathcal{L}'_n(\boldsymbol{x})$ from $\boldsymbol{x}$ to $\boldsymbol{x}_a$ and $\boldsymbol{x}_b$, respectively. $f(\omega, \mathcal{L}_m)$ and $f(\omega, \mathcal{L}'_n)$ are the amplitude of individual ray components from $\boldsymbol{x}$ to $\boldsymbol{x}_a$ and $\boldsymbol{x}_b$, respectively, which are related to the geometric spreading, the reflection and transmission coeffcients, and the attenuation, etc. It varies slowly in comparison with the phase term. $T(\boldsymbol{x}, \boldsymbol{x}_a, \mathcal{L}_m)$ and $T(\boldsymbol{x}, \boldsymbol{x}_b, \mathcal{L}'_n)$ represent the travel time from $\boldsymbol{x}$ to $\boldsymbol{x}_a$ and $\boldsymbol{x}_b$ as

$$\begin{aligned} T(\boldsymbol{x}, \boldsymbol{x}_a, \mathcal{L}_m) &= \int_{\boldsymbol{x}_a}^{\boldsymbol{x}} \boldsymbol{p}(\boldsymbol{\xi}, \mathcal{L}_m) \cdot d\boldsymbol{\xi} \\ T(\boldsymbol{x}, \boldsymbol{x}_b, \mathcal{L}'_n) &= \int_{\boldsymbol{x}_b}^{\boldsymbol{x}} \boldsymbol{p}(\boldsymbol{\xi}, \mathcal{L}'_n) \cdot d\boldsymbol{\xi} \end{aligned}, \tag{2}$$

with the slowness vectors $\boldsymbol{p}(\boldsymbol{\xi}, \mathcal{L}_m)$ and $\boldsymbol{p}(\boldsymbol{\xi}, \mathcal{L}'_n)$ along $\mathcal{L}_m$ and $\mathcal{L}'_n$, respectively. We define the ray descriptors $\mathcal{L}_m(\boldsymbol{x})$ and $\mathcal{L}'_n(\boldsymbol{x})$ as following: let an imaginary source at $\boldsymbol{x}_a$ radiate body waves with the wavefront $\Pi_1, \Pi_2, \ldots$ sweeping across V, and then, any $\boldsymbol{x}$ on Π_m corresponds to one ray $\mathcal{L}_m(\boldsymbol{x})$. Similar definitions can be performed to the ray descriptor $\mathcal{L}'_n$ and the corresponding wavefront Π'_n from an imaginary source at $\boldsymbol{x}_b$ (Figure 2). Geometric ray approximation is not valid when the caustic is around a ray path. To avoid the emergence of caustics, we assume the wavefronts keep convex when overlooked from the source.

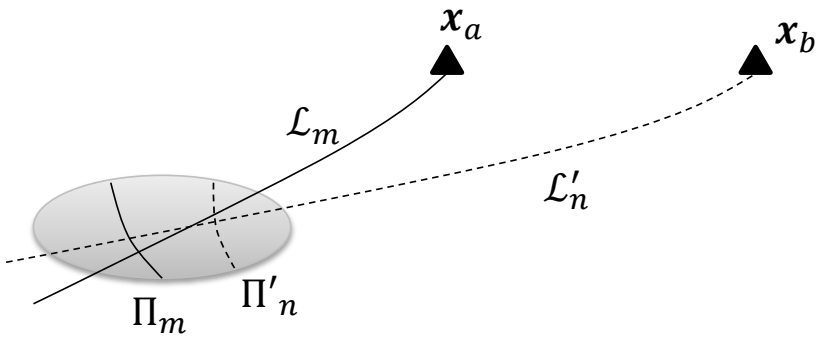

Figure 2. The rays $\mathcal{L}_m$ and $\mathcal{L}'_n$ radiated by imaginary sources at $\boldsymbol{x}_a$ and $\boldsymbol{x}_b$, respectively. The corresponding wavefronts Π_m and Π'_n are in the gray source region.

Similar to Snieder (2004) and Boschi & Weemstra (2015), we assume that the noise sources are spatially and temporally uncorrelated in V. The assumption yields

$$\langle N^*(\omega, \boldsymbol{x}) N(\omega, \boldsymbol{x}') \rangle = S(\omega, \boldsymbol{x}) \ , \tag{3}$$

where $\langle \cdot \rangle$ designates the ensemble average, and the power spectrum density $S(\omega, \boldsymbol{x})$ is a real function. Under the assumption, the body wave CCF is

$$\begin{aligned} \langle C \rangle (\omega, \boldsymbol{x}_a, \boldsymbol{x}_b) &= \int_V \int_V u^*(\omega, \boldsymbol{x}, \boldsymbol{x}_a) u(\omega, \boldsymbol{x}', \boldsymbol{x}_b) d^3x d^3x' \\ &= \int_V \langle u^*(\omega, \boldsymbol{x}, \boldsymbol{x}_a) u(\omega, \boldsymbol{x}', \boldsymbol{x}_b) \rangle \, d^3x \\ &= \sum_m \sum_n \int_V Q_{mn}(\omega, \boldsymbol{x}) e^{i\omega \psi_{mn}(\boldsymbol{x}, \boldsymbol{x}_a, \boldsymbol{x}_b)} \, d^3x \ , \end{aligned} \tag{4}$$

with

$$Q_{mn}(\omega, \boldsymbol{x}) = S(\omega, \boldsymbol{x}) f(\omega, \boldsymbol{x}, \boldsymbol{x}_a, \mathcal{L}_m) f(\omega, \boldsymbol{x}, \boldsymbol{x}_b, \mathcal{L}'_n) \ , \tag{5}$$

and

$$\psi_{mn}(\boldsymbol{x}, \boldsymbol{x}_a, \boldsymbol{x}_b) = T(\boldsymbol{x}, \boldsymbol{x}_b, \mathcal{L}'_n) - T(\boldsymbol{x}, \boldsymbol{x}_a, \mathcal{L}_m) \ . \tag{6}$$

2.2 Two types of features

The volume integral in Eq. (4) can be computed by stationary phase approximation if ω is high and $Q_{mn}(\omega, \boldsymbol{x})$ varies smoothly. In stationary phase approximation, the main contribution to the integral comes from the integral domain in which the phase remains nearly constant or stationary. If $\boldsymbol{x}_s$ is a stationary source for the correlation between seismic waves along $\mathcal{L}_m$ and $\mathcal{L}'_n$, it should satisfy

$$\nabla \psi_{mn}(\boldsymbol{x})|_{\boldsymbol{x}=\boldsymbol{x}_s} = 0 \ . \tag{7}$$

This yields

$$\boldsymbol{p}(\boldsymbol{x}_s, \mathcal{L}_m) = \boldsymbol{p}(\boldsymbol{x}_s, \mathcal{L}'_n) \ . \tag{8}$$

Given the identical initial condition, $\mathcal{L}_m(\boldsymbol{x})$ and $\mathcal{L}'_n(\boldsymbol{x})$ coincide in the smooth medium, any noise source on the coincident ray path is a stationary source. Because $\mathcal{L}_m(\boldsymbol{x})$ and $\mathcal{L}'_n(\boldsymbol{x})$ coincide in V, $\psi_{mn}(\boldsymbol{x}_s, \boldsymbol{x}_a, \boldsymbol{x}_b)$ is irrelevant to $\boldsymbol{x}_s$. We define a new function as

$$\Delta_{mn}(\boldsymbol{x}_a, \boldsymbol{x}_b) = \psi_{mn}(\boldsymbol{x}_s, \boldsymbol{x}_a, \boldsymbol{x}_b) = T(\boldsymbol{x}_s, \boldsymbol{x}_b, \mathcal{L}'_n) - T(\boldsymbol{x}_s, \boldsymbol{x}_a, \mathcal{L}_m) \ , \tag{9}$$

and there is

$$\Delta_{mn}(\boldsymbol{x}_a, \boldsymbol{x}_b) = -\Delta_{mn}(\boldsymbol{x}_b, \boldsymbol{x}_a) \ . \tag{10}$$

$\Delta_{mn}(\boldsymbol{x}_a, \boldsymbol{x}_b)$ represents the travel time difference from the stationary sources to $\boldsymbol{x}_a$ along $\mathcal{L}_m(\boldsymbol{x})$ and to $\boldsymbol{x}_b$ along $\mathcal{L}'_n(\boldsymbol{x})$, respectively. Particularly, when $\mathcal{L}_m(\boldsymbol{x})$ and $\mathcal{L}'_n(\boldsymbol{x})$ coincide until arriving $\boldsymbol{x}_a$ or $\boldsymbol{x}_b$, $\Delta_{mn}(\boldsymbol{x}_a, \boldsymbol{x}_b)$ is

$$\Delta_{mn}(\boldsymbol{x}_a, \boldsymbol{x}_b) = T(\boldsymbol{x}_a, \boldsymbol{x}_b, \mathcal{L}'_n) \ . \tag{11}$$

It is the travel time from $\boldsymbol{x}_a$ to $\boldsymbol{x}_b$ along $\mathcal{L}'_n$, i.e., the travel time of inter-station body waves.

However, seismic wave reflections and transmissions at the discontinuous interfaces can result in bifurcations of ray paths, so $\mathcal{L}_m(\boldsymbol{x})$ and $\mathcal{L}'_n(\boldsymbol{x})$ are not necessarily coincident outside V (Figure 3). The two scenarios (with and without ray bifurcations) divide the correlation signals into two types of features — resembling the inter-station body waves and the spurious waves at the travel time difference between the conventional reflections. The dominant contributions of the two types of features are body waves with the same emitting slowness vector, which is similar to Kennett & Pham (2018) that coda waves of the same slowness contribute to the two types of features. However, here excludes the correlation between P and S waves because they do not have the same take-off angle when radiating with the same slowness.

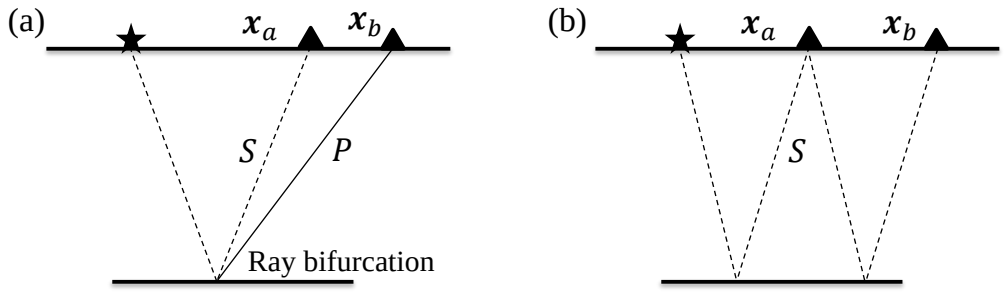

Figure 3. (a) A ray bifurcation at the discontinuous interface from S (dash) to S and P (solid) waves; (b) without bifurcations.

2.3 The Stationary Integral

At $\boldsymbol{x}_s$, the phase term $\psi_{mn}(\boldsymbol{x})$ can be expanded with Taylor's series as

$$\psi_{mn}(\boldsymbol{x}, \boldsymbol{x}_a, \boldsymbol{x}_b) = \Delta_{mn}(\boldsymbol{x}_a, \boldsymbol{x}_b) + \frac{1}{2}(\boldsymbol{x} - \boldsymbol{x}_s)^T \boldsymbol{H}_{mn}(\boldsymbol{x}_s)(\boldsymbol{x} - \boldsymbol{x}_s) + \cdots \ . \tag{12}$$

In Eq. (12), the Hessian matrix $\boldsymbol{H}_{mn}(\boldsymbol{x}_s)$ is

$$\boldsymbol{H}_{mn}(\boldsymbol{x}_s) = \nabla\nabla\psi_{mn}(\boldsymbol{x})|_{\boldsymbol{x}=\boldsymbol{x}_s} \ . \tag{13}$$

In Appendix Appendix A, $\boldsymbol{H}_{mn}(\boldsymbol{x}_s)$ is diagonalizable with real eigenvalues and eigenvectors as

$$\boldsymbol{H}_{mn}(\boldsymbol{x}_s) = \boldsymbol{E}^T_{mn}(\boldsymbol{x}_s)\boldsymbol{\Lambda}_{mn}(\boldsymbol{x}_s)\boldsymbol{E}_{mn}(\boldsymbol{x}_s) \ , \tag{14}$$

with the superscript T denoting transpose of the matrix. The coordinate transformation matrix is

$$\boldsymbol{E}_{mn}(\boldsymbol{x}_s) = [\hat{\boldsymbol{\eta}}_1(\boldsymbol{x}_s), \hat{\boldsymbol{\eta}}_2(\boldsymbol{x}_s), \hat{\boldsymbol{\eta}}_3], \tag{15}$$

with the unit vector $\hat{\boldsymbol{\eta}}_3$ along the ray path. $\hat{\boldsymbol{\eta}}_1(\boldsymbol{x}_s)$ and $\hat{\boldsymbol{\eta}}_2(\boldsymbol{x}_s)$ correspond to the steepest and slowness descent direction of the distance difference at $\boldsymbol{x}_s$, where the distances are from Π_m and Π'_n to the common tangent plane of the two wavefronts, respectively. $\hat{\boldsymbol{\eta}}_1(\boldsymbol{x}_s)$ and $\hat{\boldsymbol{\eta}}_2(\boldsymbol{x}_s)$ usually vary in V when the outside is inhomogeneous (Figure 4). In a laterially homogeneous medium, $\hat{\boldsymbol{\eta}}_1$ and $\hat{\boldsymbol{\eta}}_2$ correspond to the SV and SH direction, respectively. The diagonal matrix $\boldsymbol{\Lambda}_{mn}(\boldsymbol{x}_s)$ is

$$\begin{aligned}\boldsymbol{\Lambda}_{mn}(\boldsymbol{x}_s) =& \mathrm{diag}\{\nu_1^{(mn)}(\boldsymbol{x}_s), \nu_2^{(mn)}(\boldsymbol{x}_s), 0\} \\ =& \frac{1}{c}\begin{bmatrix} \kappa_1(\boldsymbol{x}_s, \mathcal{L}'_n) - \kappa_1(\boldsymbol{x}_s, \mathcal{L}_m) & 0 & 0 \\ 0 & \kappa_2(\boldsymbol{x}_s, \mathcal{L}'_n) - \kappa_2(\boldsymbol{x}_s, \mathcal{L}_m) & 0 \\ 0 & 0 & 0 \end{bmatrix},\end{aligned} \tag{16}$$

with $c = \alpha$ or β. $\kappa_1(\boldsymbol{x}_s, \mathcal{L}_m)$ and $\kappa_1(\boldsymbol{x}_s, \mathcal{L}'_n)$ represent the curvature of curves at $\boldsymbol{x}_s$ in the η_1 direction on Π_m and Π'_n, respectively, so are $\kappa_2(\boldsymbol{x}_s, \mathcal{L}_m)$ and $\kappa_2(\boldsymbol{x}_s, \mathcal{L}'_n)$ except in the η_2 direction.

In the Frenet frame $\{\boldsymbol{x}_s; \hat{\boldsymbol{\eta}}_1(\boldsymbol{x}_s), \hat{\boldsymbol{\eta}}_2(\boldsymbol{x}_s), \hat{\boldsymbol{\eta}}_3\}$, the stationary points are at $(0, 0, \eta_3)$. The source region is $V = \widetilde{L}_1^{(mn)}(\eta_2, \eta_3) \times \widetilde{L}_2^{(mn)}(\eta_3) \times \widetilde{L}_3^{(mn)}$, with $\widetilde{L}_1^{(mn)}$, $\widetilde{L}_2^{(mn)}$ and $\widetilde{L}_3^{(mn)}$ representing the geometric intervals of noise source distribution in the η_1, η_2 and η_3 direction, respectively.

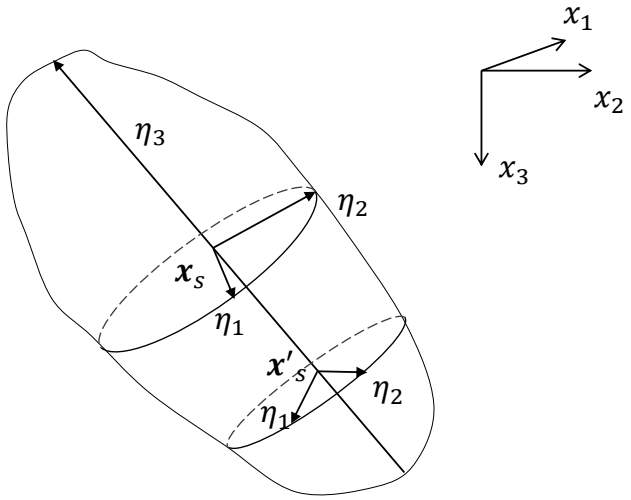

Figure 4. The η_1, η_2 and η_3 direction in the homogeneous source region (gray). η_1 and η_2 have rotated around η_3 from $\boldsymbol{x}_s$ to $\boldsymbol{x}'_s$.

We substitute Eq. (12) into (4) and asymptotically compute the CCF as

$$\begin{aligned}\langle C\rangle(\omega,\boldsymbol{x}_a,\boldsymbol{x}_b) =& \sum_m\sum_n \int_V Q_{mn}(\omega,\boldsymbol{x}) e^{i\omega\psi_{mn}(\boldsymbol{x},\boldsymbol{x}_a,\boldsymbol{x}_b)}\, d^3x \\ =& \sum_m\sum_n e^{i\omega\Delta_{mn}(\boldsymbol{x}_a,\boldsymbol{x}_b)} \int_{\widetilde{L}_3^{(mn)}} Q_{mn}(\omega,\eta_3) \int_{\widetilde{L}_2^{(mn)}}\int_{\widetilde{L}_1^{(mn)}} e^{\frac{i\omega}{2}\boldsymbol{\eta}^T\boldsymbol{\Lambda}_{\boldsymbol{mn}}(\eta_3)\boldsymbol{\eta}}\, d^3\eta \\ =& \sum_m\sum_n e^{i\omega\Delta_{mn}(\boldsymbol{x}_a,\boldsymbol{x}_b)} \int_{\widetilde{L}_3^{(mn)}} \frac{2Q_{mn}(\omega,\eta_3)\Gamma_{mn}(\eta_3)}{\omega\sqrt{|\nu_1^{(mn)}(\eta_3)\nu_2^{(mn)}(\eta_3)|}}\, d\eta_3\ ,\end{aligned} \tag{17}$$

where

$$\begin{aligned}\Gamma_{mn}(\eta_3) =& \frac{\omega}{2}\sqrt{|\nu_1^{(mn)}(\eta_3)\nu_2^{(mn)}(\eta_3)|}\int_{\widetilde{L}_2^{(mn)}}\int_{\widetilde{L}_1^{(mn)}} e^{\frac{i\omega}{2}\boldsymbol{\eta}^T\boldsymbol{\Lambda}_{\boldsymbol{mn}}(\eta_3)\boldsymbol{\eta}}\, d\eta_1 d\eta_2 \\ =& \int_{\widetilde{L}_2'^{(mn)}} e^{i\eta_2'^2\mathrm{sgn}[\nu_2^{(mn)}(\eta_3)]}\int_{\widetilde{L}_1'^{(mn)}} e^{i\eta_1'^2\mathrm{sgn}[\nu_1^{(mn)}(\eta_3)]}\, d\eta_1' d\eta_2'\ .\end{aligned} \tag{18}$$

with $\widetilde{L}_1'^{(mn)} = \gamma_1^{(mn)}\widetilde{L}_1^{(mn)}$,$\widetilde{L}_2'^{(mn)} = \gamma_2^{(mn)}\widetilde{L}_2^{(mn)}$ and

$$\begin{aligned}\gamma_1^{(mn)} =& \sqrt{\frac{\omega|\nu_1^{(mn)}(\eta_3)|}{2}} = \sqrt{k|\kappa_1(\boldsymbol{x}_s,\mathcal{L}_n') - \kappa_1(\boldsymbol{x}_s,\mathcal{L}_m)|/2} \\ \gamma_2^{(mn)} =& \sqrt{\frac{\omega|\nu_2^{(mn)}(\eta_3)|}{2}} = \sqrt{k|\kappa_2(\boldsymbol{x}_s,\mathcal{L}_n') - \kappa_2(\boldsymbol{x}_s,\mathcal{L}_m)|/2}\end{aligned}\ . \tag{19}$$

$k = \omega/c$ represents the seismic wavenumber in V. We name $\gamma_1^{(mn)}$ and $\gamma_2^{(mn)}$ as the k-κ coefficients according to the physical parameters contained. Correspondingly, we name $\widetilde{L}_1'^{(mn)} \times \widetilde{L}_2'^{(mn)}$ as the k-κ interval, in contrast with the geometric interval $\widetilde{L}_1^{(mn)} \times \widetilde{L}_2^{(mn)}$. The comparison of the two intervals is shown in Figure 5. In Eq. (18), the double integral is related to the Fresnel integral as

$$F(x) = |F(x)|e^{i\Theta(x)} = \int_0^x e^{it^2}\, dt\ . \tag{20}$$

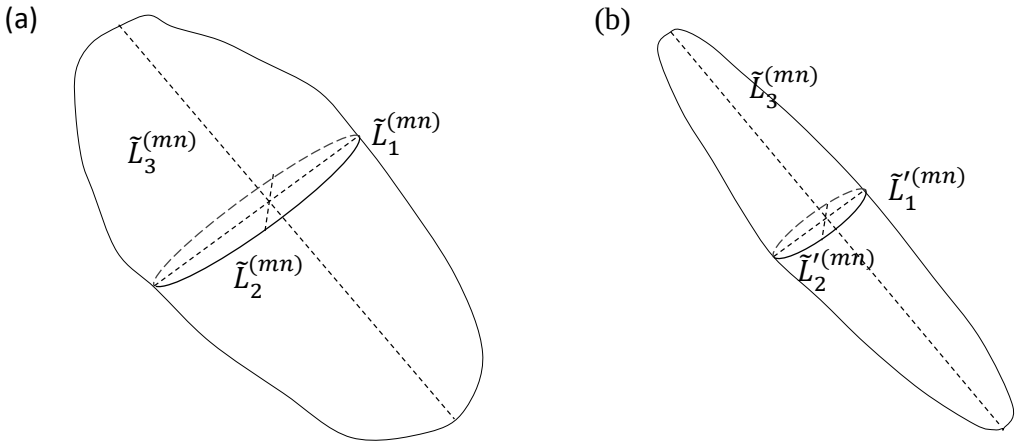

Figure 5. (a) The geometric interval $\widetilde{L}_1^{(mn)} \times \widetilde{L}_2^{(mn)} \times \widetilde{L}_3^{(mn)}$; (b) the k-κ interval $\widetilde{L}_1'^{(mn)} \times \widetilde{L}_2'^{(mn)} \times \widetilde{L}_3^{(mn)}$. $\widetilde{L}_3^{(mn)}$ is not changed in the two intervals.

When $x \to +\infty$, it gives

$$F(+\infty) = \int_0^{+\infty} e^{it^2}\, dt = \frac{\sqrt{\pi}}{2} e^{i\pi/4}\ . \tag{21}$$

While x is not so large, the amplitude and phase of the Fresnel integral are shown in Figure 6. The phase of the Fresnel integral is nearly 0 while $x \to 0$, and it converges to $\pi/4$ oscillatorily as x increases. Therefore, $\Gamma_{mn}(\eta_3)$ only results in constrained phase variations in Eq. (17), approximately within $\pi/2$.

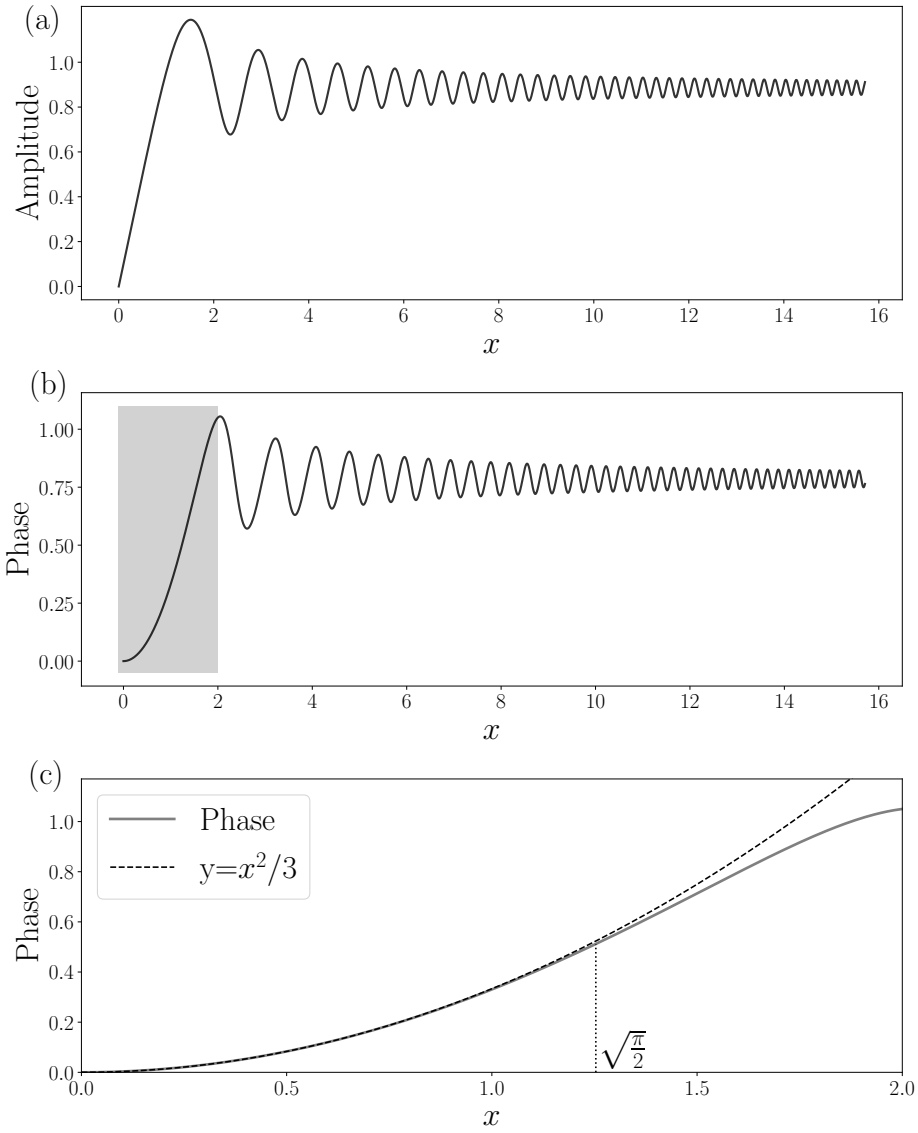

Figure 6. The Fresnel integral: (a) the amplitude, (b) the phase, and (c) approximation of the phase term by the quadratic function $y = x^2/3$.

2.4 A Large k-κ Interval

When $\widetilde{L}_1'^{(mn)}(\eta_2,\eta_3)\times\widetilde{L}_2'^{(mn)}(\eta_3)\supset(-1/\epsilon,1/\epsilon)\times(-1/\epsilon,1/\epsilon)$, with ϵ extremely small, it gives

$$\Gamma_{mn}(\eta_3)=\pi e^{\frac{i\pi}{4}\left\{\mathrm{sgn}[\nu_1^{(mn)}(\eta_3)]+\mathrm{sgn}[\nu_2^{(mn)}(\eta_3)]\right\}}\ . \tag{22}$$

Substituting it into Eq. (17) gives

$$\begin{aligned}\langle C\rangle(\omega,\boldsymbol{x}_a,\boldsymbol{x}_b)=&\sum_m\sum_n e^{i\omega\Delta_{mn}(\boldsymbol{x}_a,\boldsymbol{x}_b)}\\&\times\int_{\widetilde{L}_3^{(mn)}}\frac{2\pi Q(\omega,\eta_3)}{\omega\sqrt{|\nu_1^{(mn)}(\eta_3)\nu_2^{(mn)}(\eta_3)|}}e^{\frac{i\pi}{4}\left\{\mathrm{sgn}[\nu_1^{(mn)}(\eta_3)]+\mathrm{sgn}[\nu_2^{(mn)}(\eta_3)]\right\}}d\eta_3\ .\end{aligned} \tag{23}$$

When $\mathcal{L}_m$ and $\mathcal{L}_n'$ coincide before arriving $\boldsymbol{x}_a$ or $\boldsymbol{x}_b$, the correlation waves correspond to the inter-station body waves. For the convex wavefronts Π_m and Π_n', in Appendix B, we obtain

$$\mathrm{sgn}[\nu_1^{(mn)}(\eta_3)],\mathrm{sgn}[\nu_2^{(mn)}(\eta_3)]=\begin{cases}-1\ , & \boldsymbol{x}_s\in V_-\\ 1\ , & \boldsymbol{x}_s\in V_+\end{cases}\ . \tag{24}$$

Substituting it into Eq. (23), we obtain the correlation signals that converge the inter-station body waves as

$$\begin{aligned}\left\langle C^{(g)}\right\rangle(\omega,\boldsymbol{x}_a,\boldsymbol{x}_b)=&\sum_m\sum_n\int_{\widetilde{L}_{3-}^{(mn)}}\frac{2\pi Q(\omega,\eta_3)}{\sqrt{\nu_1^{(mn)}(\eta_3)\nu_2^{(mn)}(\eta_3)}}d\eta_3\cdot\frac{e^{i\omega T(\boldsymbol{x}_a,\boldsymbol{x}_b,\mathcal{L}_n')}}{i\omega}\\&+\sum_m\sum_n\int_{\widetilde{L}_{3+}^{(mn)}}\frac{2\pi Q(\omega,\eta_3)}{\sqrt{\nu_1^{(mn)}(\eta_3)\nu_2^{(mn)}(\eta_3)}}d\eta_3\cdot\left\{\frac{e^{i\omega T(\boldsymbol{x}_b,\boldsymbol{x}_a,\mathcal{L}_n')}}{i\omega}\right\}^*\ .\end{aligned} \tag{25}$$

When the k-κ interval is large, the correlation signals can precisely recover the phase of Green's function for displacement, consistent with the existing theories (Boschi & Weemstra, 2015; Fichtner & Tsai, 2019). Besides the source and propagation terms, the integrand function for the correlation amplitude is inversely proportional to $\omega\sqrt{\nu_1^{(mn)}(\eta_3)\nu_2^{(mn)}(\eta_3)}/2$, i.e., the k-κ coefficients $\gamma_1^{(mn)}\times\gamma_2^{(mn)}$. Therefore, the dimension of the stationary phase zone is also related to the correlation amplitude.

2.5 A Small k-κ Interval

For the seismic cross-correlation at nearby stations on the Earth's surface, direct body waves and near-surface reflections travel horizontally, so the $\eta_1\eta_2$ plane is nearly perpendicular to the Earth's surface and is limited at the depth direction due to a near-surface distribution of earthquakes; while the reflections from the deep Earth's discontinuities travel vertically, so the $\eta_1\eta_2$ plane is parallel to the surface (Figure 7). Here, we discuss the situation when earthquakes are in a small region.

For simplicity, we consider a square geometric $\eta_1\eta_2$ plane as $\widetilde{L}_1^{(mn)}(\eta_2,\eta_3)\times\widetilde{L}_2^{(mn)}(\eta_3) = \{[-\bar{\eta}_1(\eta_3),\bar{\eta}_1(\eta_3)]\times[-\bar{\eta}_2(\eta_3),\bar{\eta}_2(\eta_3)]\}$. We denote $\bar{\eta'}_1 = \gamma_1^{(mn)}\bar{\eta}_1$ and $\bar{\eta'}_2 = \gamma_2^{(mn)}\bar{\eta}_2$. It gives

$$\Gamma_{mn}(\eta_3) = 4|F(\bar{\eta'}_1)F(\bar{\eta'}_2)|e^{i[\Theta(\bar{\eta'}_1)+\Theta(\bar{\eta'}_2)]} \ , \tag{26}$$

Expanding the phase term of the Fresnel integral with Taylor's series, we can approximate $\Theta(\bar{\eta'}_1)$ and $\Theta(\bar{\eta'}_2)$ as

$$\begin{aligned}\Theta(\bar{\eta'}_1) \approx& \frac{\bar{\eta'}_1^2\mathrm{sgn}[\nu_1^{(mn)}]}{3} = \frac{\omega\nu_1^{(mn)}\bar{\eta}_1^2}{3} \\ \Theta(\bar{\eta'}_2) \approx& \frac{\omega\nu_2^{(mn)}\bar{\eta}_2^2}{3}\end{aligned} \ . \tag{27}$$

In Figure 6c, the approximation is precise when $\bar{\eta'}_1^2 \in (0,\pi/2)$ and $\bar{\eta'}_2 \in (0,\pi/2)$. We obtain

$$\Theta(\bar{\eta'}_1) + \Theta(\bar{\eta'}_2) \approx \omega\tau^{(mn)}(\eta_3) \ , \tag{28}$$

with

$$\tau^{(mn)}(\eta_3) = \frac{1}{3}[\nu_1^{(mn)}\bar{\eta}_1^2 + \nu_2^{(mn)}\bar{\eta}_2^2] \ . \tag{29}$$

Substituting it and Eq. (26) into (17), it gives

$$\langle C\rangle(\omega,\boldsymbol{x}_a,\boldsymbol{x}_b) \approx \sum_m\sum_n\int_{\widetilde{L}_3^{(mn)}} \frac{8Q_{mn}(\omega,\eta_3)|F(\bar{\eta'}_1)F(\bar{\eta'}_2)|}{\omega\sqrt{|\nu_1^{(mn)}(\eta_3)\nu_2^{(mn)}(\eta_3)|}} e^{i\omega[\Delta_{mn}(\boldsymbol{x}_a,\boldsymbol{x}_b)+\tau^{(mn)}(\eta_3)]}\,d\eta_3 \ . \tag{30}$$

For the correlation signals convergent to inter-station body waves, it gives

$$\begin{aligned}\left\langle C^{(g)}\right\rangle(\omega,\boldsymbol{x}_a,\boldsymbol{x}_b) \approx& \sum_m\sum_n\int_{\widetilde{L}_{3-}^{(mn)}} \frac{8Q_{mn}(\omega,\eta_3)|F(\bar{\eta'}_1)F(\bar{\eta'}_2)|}{\omega\sqrt{|\nu_1^{(mn)}(\eta_3)\nu_2^{(mn)}(\eta_3)|}} e^{i\omega[T(\boldsymbol{x}_a,\boldsymbol{x}_b,\mathcal{L}'_n)+\tau^{(mn)}(\eta_3)]}\,d\eta_3 \\ &+ \sum_m\sum_n\int_{\widetilde{L}_{3+}^{(mn)}} \frac{8Q_{mn}(\omega,\eta_3)|F(\bar{\eta'}_1)F(\bar{\eta'}_2)|}{\omega\sqrt{|\nu_1^{(mn)}(\eta_3)\nu_2^{(mn)}(\eta_3)|}} \left\{e^{i\omega[T(\boldsymbol{x}_b,\boldsymbol{x}_a,\mathcal{L}'_n)-\tau^{(mn)}(\eta_3)]}\right\}^* d\eta_3 \ ,\end{aligned} \tag{31}$$

with

$$\begin{cases}\tau^{(mn)}(\eta_3) < 0 \ , & \boldsymbol{x}_s \in V_- \\ \tau^{(mn)}(\eta_3) > 0 \ , & \boldsymbol{x}_s \in V_+\end{cases} \ . \tag{32}$$

when the k-κ interval is small, the correlation signals can recover the phase of the inter-station body waves for velocity, along with a few arrival time advances. The integrand function for the correlation amplitude is a little complex. It is inversely proportional to the k-κ coefficients, but proportional to the Fresnel amplitude. The Fresnel integral is a function of the k-κ interval, so the amplitude is related to the distribution geometry of earthquakes.

Let $\bar{\eta'}_1^2 \le \pi/2$ and $\bar{\eta'}_2^2 \le \pi/2$, i.e.,

$$\omega|\nu_1^{(mn)}|\bar{\eta}_1^2 \le \frac{\pi}{2} \quad \text{and} \quad \omega|\nu_1^{(mn)}|\bar{\eta}_1^2 \le \frac{\pi}{2} \ . \tag{33}$$

In the k-κ interval, the correlation phase varies slowly as the quadratic function. On the contrary, the fitting of the correlation phase requires high-order terms of Taylor's series, which means a rapid phase change for earthquakes outside the interval. Therefore, we can utilize the k-κ interval to determine the stationary phase zone. In practice, the vectors $\hat{\boldsymbol{\eta}}_1$ and $\hat{\boldsymbol{\eta}}_2$ are usually difficult to constrain. For simplicity, we disregard the directions and conservatively define the stationary phase zone as a circle in the $\eta_1\eta_2$ plane with the center at the stationary point and the radius of $\min\{\sqrt{\pi/2}/\gamma_1^{(mn)}, \sqrt{\pi/2}/\gamma_2^{(mn)}\}$. In the stationary phase zone, we estimate

$$|\tau^{(mn)}(\eta_3)| \sim \frac{\pi}{3\omega} = \frac{T_0}{6} \ , \tag{34}$$

with T_0 designating the coda wave period. The travel time variation can reach 1/6 of the body wave correlation period. For instance, for coda waves in the period around 10 s, the event-receiver geometry can result in a emergence time advance within 1.7 s.

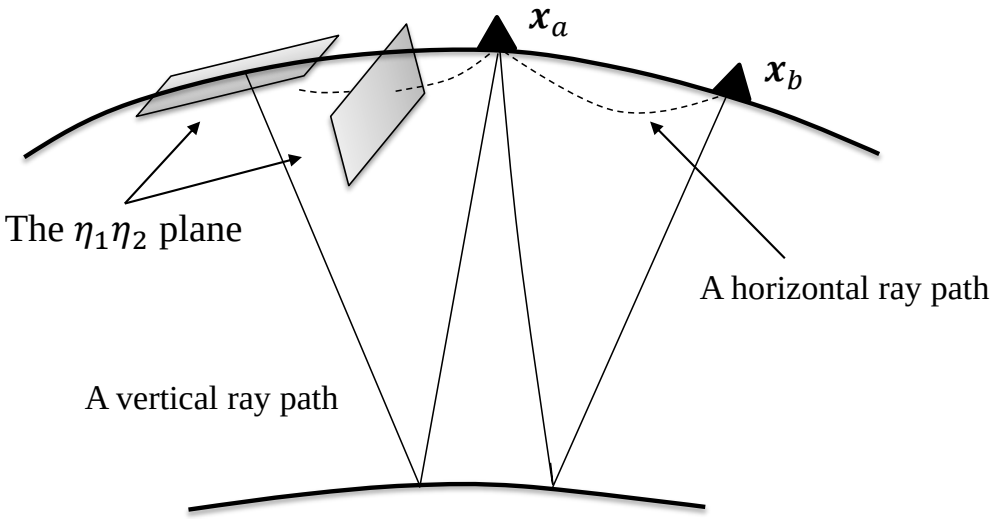

Figure 7. The horizontally (dash) and vertically (solid) travelling body waves. The triangles represent two stations $\boldsymbol{x}_a$ and $\boldsymbol{x}_b$. The different $\eta_1\eta_2$ planes are shown.

3 Late Coda Correlations

3.1 Theoretical Analysis

In the section, we use the current theoretical results to interpret the correlation signals that converge to the inter-station body waves. In theory, these features are constructed by correlating coda waves from earthquakes around the extended inter-station ray paths. The k-κ interval strongly influences the correlation phase variations. The dimensionless k-κ interval contains the geometric interval of earthquake distributions and the k-κ coefficient.

The k-κ coefficient is related to the curvature of curves on the coda wavefront, namely the coda propagation distance, so it determines the dimension of the stationary phase zone. In the realistic coda correlations, large earthquakes are basically discrete in the continental boundaries and mostly do not situate at the extended ray paths connecting two stations. More seriously, one inter-station ray path may correspond to many extended ray paths, and the earthquake situating at one extended ray path may deviate from others (Figure 8a). Therefore, the total contribution even from one earthquake is difficult to predict. Here, based on the knowledge of the k-κ coefficient, we present a statistical understanding of late coda correlations.

In the k-κ coefficients, the curvature of curves on wavefronts can be approximated as

$$\begin{aligned} \kappa_1(\boldsymbol{x}_s, \mathcal{L}_m) \approx \kappa_2(\boldsymbol{x}_s, \mathcal{L}_m) \approx \frac{1}{R_a(\boldsymbol{x}_s, \mathcal{L}_m)} \\ \kappa_1(\boldsymbol{x}_s, \mathcal{L}'_n) \approx \kappa_2(\boldsymbol{x}_s, \mathcal{L}'_n) \approx \frac{1}{R_b(\boldsymbol{x}_s, \mathcal{L}'_n)} \end{aligned} , \tag{35}$$

where $R_a(\boldsymbol{x}_s, \mathcal{L}_m)$ and $R_b(\boldsymbol{x}_s, \mathcal{L}'_n)$ represent the propagation distances along $\mathcal{L}_m$ from $\boldsymbol{x}_s$ to $\boldsymbol{x}_a$, and along $\mathcal{L}'_n$ from $\boldsymbol{x}_s$ to $\boldsymbol{x}_b$, respectively. The approximation is precise when multiple reflections are confined in a homogeneous medium. Under the approximation, the k-κ coefficients are

$$\gamma_1^{(mn)} \approx \gamma_2^{(mn)} \approx \sqrt{\frac{\pi |R_b(\boldsymbol{x}_s, \mathcal{L}'_n) - R_a(\boldsymbol{x}_s, \mathcal{L}_m)|}{\lambda R_a(\boldsymbol{x}_s, \mathcal{L}_m) R_b(\boldsymbol{x}_s, \mathcal{L}'_n)}} , \tag{36}$$

where λ is the seismic wavelength in the source region.

In the late coda correlations, researchers usually use coda energy in the time interval, for example, from 20,000 to 40,000 s after the origin of large earthquakes (Lin et al., 2013). Here, we take the retrieval of the ScS wave as an example. The average S wave velocity approximates 5 km/s in the mantle. If the coda wave is at the 10 s period and has reverberated for 20,000 s, we can estimate that

$$\begin{aligned} R_a(\boldsymbol{x}_s, \mathcal{L}_m) \approx R_b(\boldsymbol{x}_s, \mathcal{L}'_n) \approx 100,000\ (km) \\ |R_a(\boldsymbol{x}_s, \mathcal{L}_m) - R_b(\boldsymbol{x}_s, \mathcal{L}'_n)| \approx 6,000\ (km) \end{aligned} . \tag{37}$$

It means that the coda correlations are processed at two stations with an inter-station propagation distance 6,000 km, and the coda waves are radiated by an earthquake 100,000 km away (Figure 8b). Thus, the k-κ coefficients are

$$\gamma_1^{(mn)} \approx \gamma_2^{(mn)} \approx 2 \times 10^{-4}\ (km^{-1}) . \tag{38}$$

Because the k-κ coefficients are very small, most of the large earthquakes situate in the stationary phase zone for the inter-station ray path even if the earthquakes are far from the stationary points in geometry. Moreover, a wide spatial distribution of earthquakes may correspond to a very narrow k-κ interval. For instance, the coda phase does not have a

rapid change at 0.1 Hz for d in the range of $5,000 - 10,000\ km$, as compared with the coda phase change at 3.0 Hz (Figure 8c). Due to these effects, the correlation of late codas from the earthquakes have a coherent addition for every inter-station ray path. However, the correlation signals may appear earlier than the inter-station body waves because the earthquakes are not always at the stationary points.

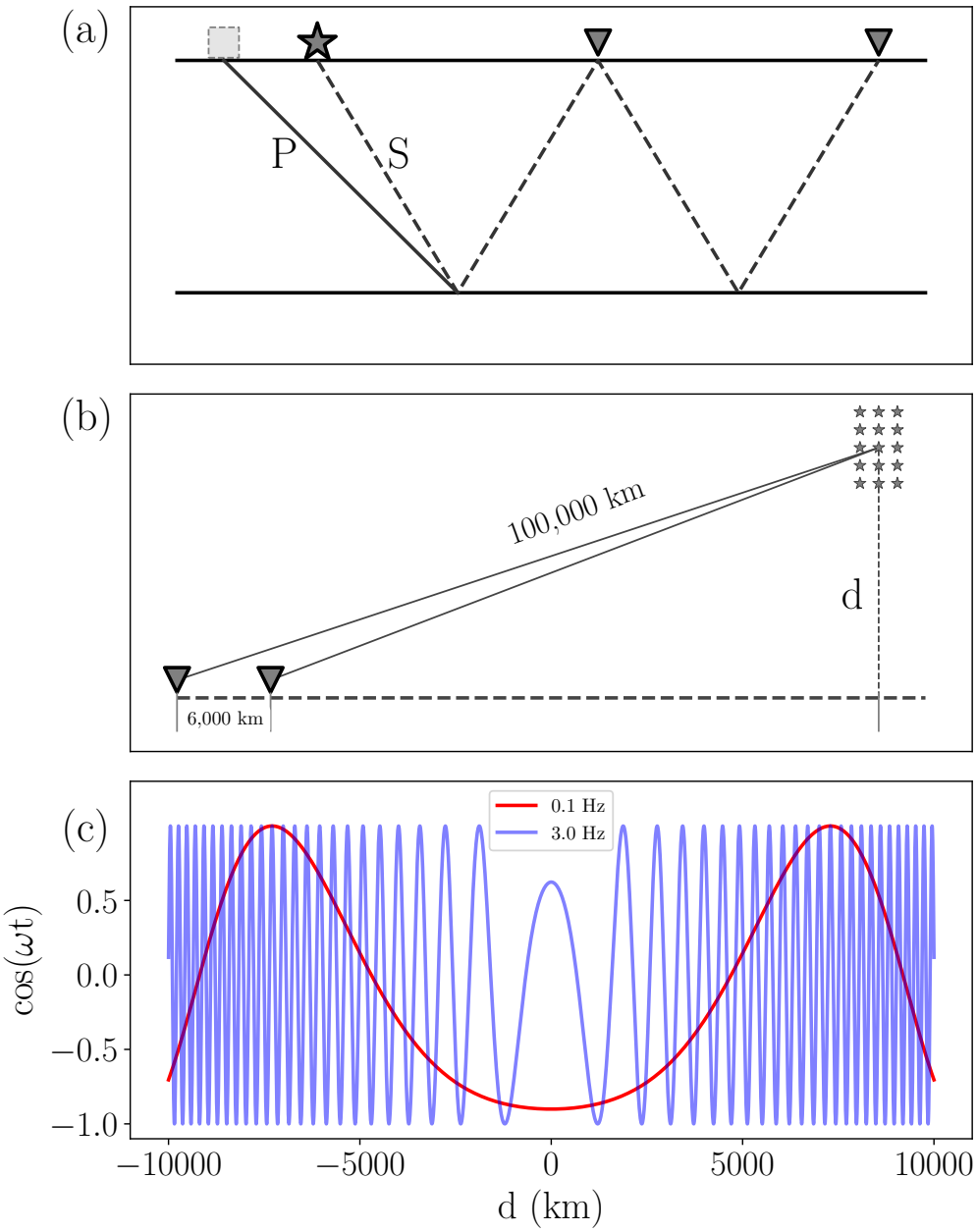

Figure 8. (a) Two extended inter-station ray paths. The dashed and solid lines represent S and P waves, respectively. The earthquake (star) is at a stationary point at one extended ray path, but not at the other. The dashed grey box represents one stationary point. (b) A schematic configuration of coda correlations. Coda waves have propagated for 100,000 km from earthquakes (star) to stations (triangle); d represents the distance from earthquakes to the stationary point in the $\eta_1\eta_2$ plane; the equivalent inter-station propagation distance is about 6000 km for the ScS wave. (c) The phase variations around the stationary point for coda correlations in the frequency of 0.1 Hz (red) and 3.0 Hz (blue).

3.2 The Simulation Verification

To verify the theoretical analysis, we carry out a numerical experiment on late earthquake coda correlations, based on the spherically stratified 1-D IASP91 model (Kennett & Engdahl, 1991). We virtualize 80 seismic stations on the equator from 80° W to 1° W in every 1° interval, and three earthquakes A, B and C at (20° E, 0° N), (20° E, 30° N) and (20° E, 60° N), respectively (Figure 9). Due to the spherical symmetry of the structure, seismic waves propagating between two stations are confined in the equatorial plane. Therefore, the stationary points are in the equator plane which are far from Earthquake B and C in geometry. The three earthquakes are at the 500 km depth, with the same focal mechanism (Figure 9).

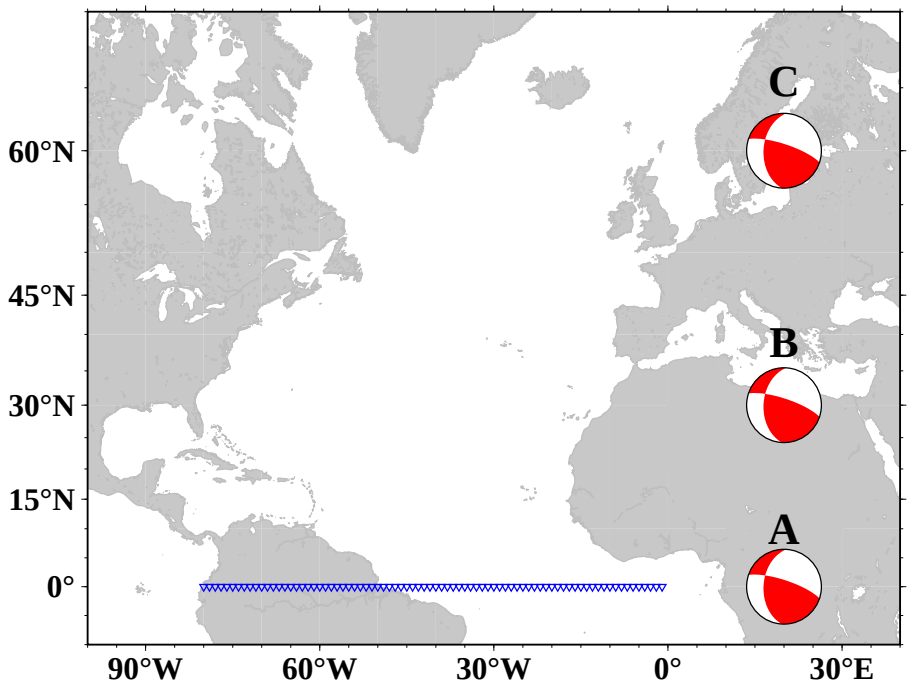

Figure 9. The source-station geometry in the simulation. A linear-shaped seismic array composed of 80 virtual stations is placed on the equator from 80° W to 1° W in every 1° interval (blue inverted triangle). Three virtual earthquakes A, B and C (the beachball center) locate at (20° E, 0° N), (20° E, 30° N) and (20° E, 60° N), respectively. The red beachballs indicate the same focal mechanism of earthquakes A, B and C.

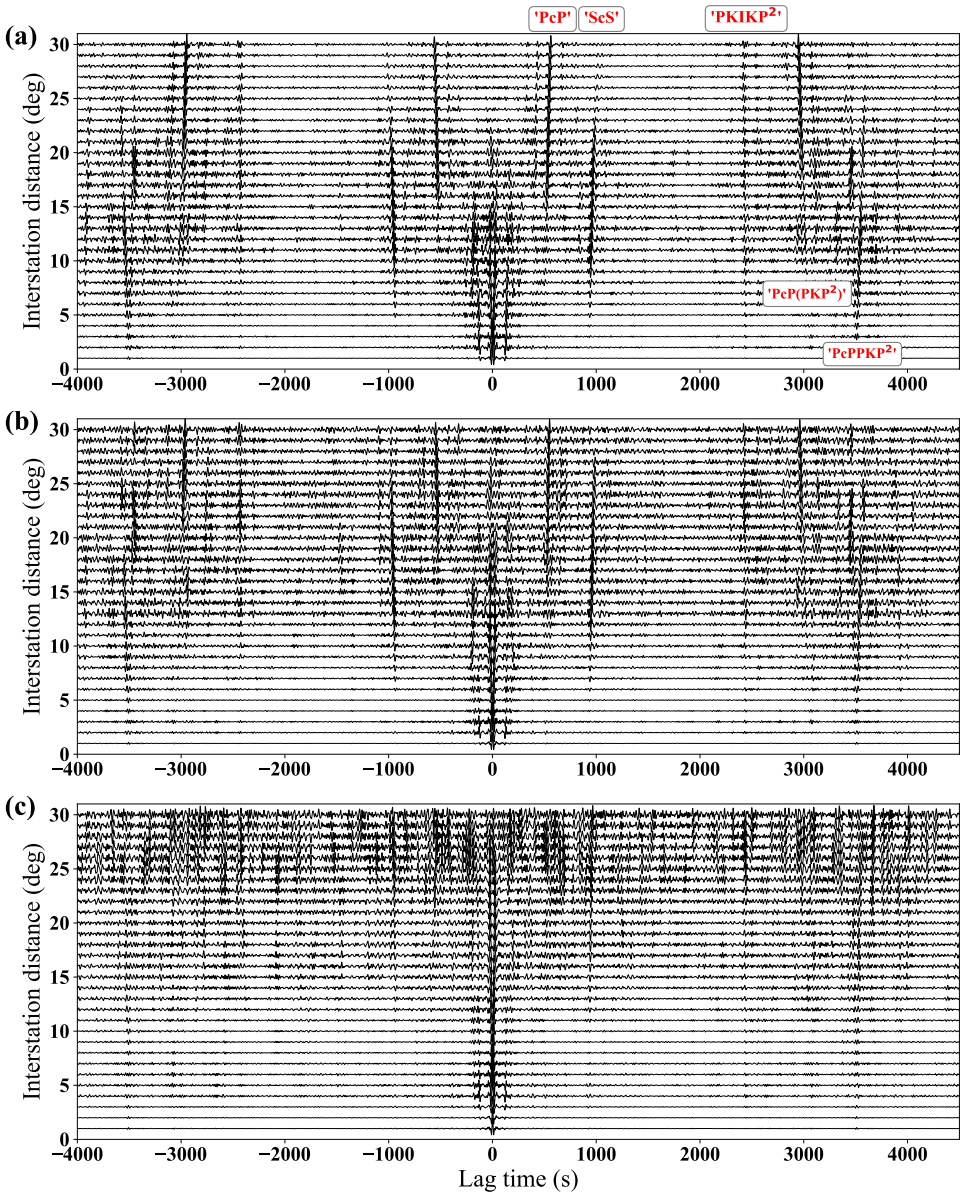

Figure 10. The synthetic normalized CCFs of coda waves from (a) Earthquake A, (b) Earthquake B, and (c) Earthquake C. Some correlation signals resembling the Earth's core phases are labelled in (a).

In the coda correlation, we adhere to the following steps: firstly, we use the direct solution method (Kawai et al., 2006) to synthesize seismograms excited by the three earthquakes, with one sample per second and 65,535-second duration; secondly, we process coda correlations closely following the similar procedures suggested by Bensen et al. (2007): cut coda wave records from 8,000 to 28,000 seconds after the origin of earthquakes; perform

band-pass filtering with the dominant band of 15−50 seconds for retrieving core phases (Lin & Tsai, 2013); suppress the records by temporal normalization with the running absolute mean rule and spectral whitening. We separately compute the normalized CCFs for every earthquake by using late codas in the time window 8,000 − 28,000 s. Finally, for each earthquake, we stack the CCFs at every one-degree inter-station distance bin to enhance the signal-to-noise ratio of correlation signals.

Several correlation signals resembling the core phases have been extracted at the negative and positive lag time windows, including ScS, $PKIKP^2$, PcP, $PcP(PKP)^2$ and $PKPPcP^2$ wave (Figure 10). Despite the long distances from earthquake B and C to the stationary points, the two earthquakes situate at the stationary phase zone because the corresponding k-κ coefficients are sufficiently small for various inter-station ray paths. Therefore, late coda correlations from the two earthquakes can also produce the correlation features, consistent with the theoretical analysis. Earthquake B and C are further from the stationary points in comparison with Earthquake A, so the correlation signals appear earlier, as in the lag time windows around the ScS arrivals (Figure 11). The large emgerence time discrepancy between Earthquake A and C suggests that late coda correlations from earthquakes far from the stationary point may result in extensive time devitations.

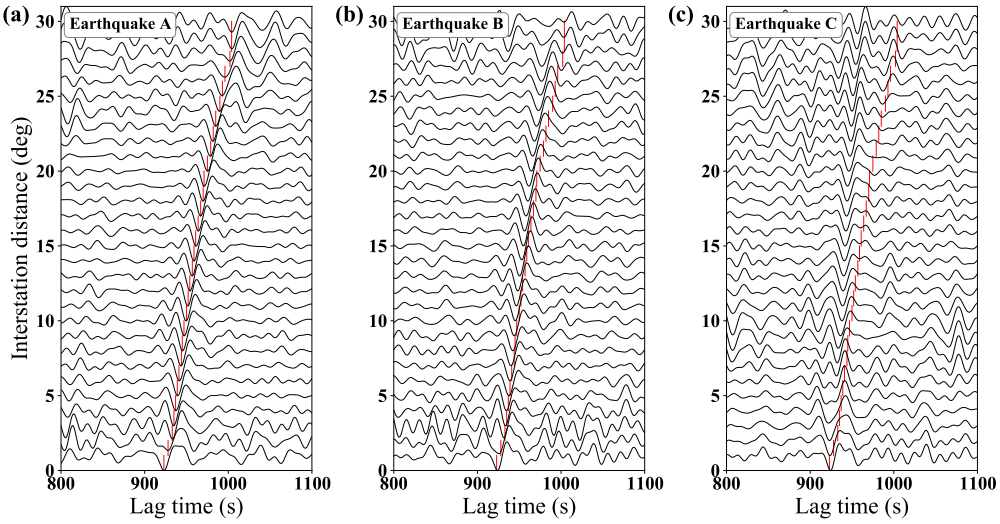

Figure 11. The CCF windows around the ScS arrivals for (a) Earthquake A, (b) Earthquake B, and (c) Earthquake C. The red vertical lines represent the emergence times near ScS wave from the correlation of coda waves released by Earthquake A.

3.3 The Realistic Coda Correlations

In the theoretical analysis and numerical simulation, we show that most of the large earthquakes situate at the stationary phase zone for the inter-station ray path in late coda correlations. In applications, researchers usually stack the correlation signals from different earthquakes to gain the CCF. Thus, the distribution geometry of earthquakes affect the correlation phase in the CCF. When stacking the interferometric seismograms in the network of dense stations according to the inter-station distance bins, if the used earthquake are abandant, the CCF stacked by station-pairs in different azimuth amounts to the CCF between one station-pair from earthquakes that rotatably appear in all azimuth. Such a created earthquake distribution is similar to the situation in Section 2.5. Here we compare the theoretical prediction and the realistic time variations caused by the earthquake distribution. Because the exact Green's function arrivals are unknown in practice, here we compare the CCFs that have been affected by different source-receiver geometries. we collect LHZ component coda waves from 205 large earthquakes ($\geq M6.8$) recorded by the permanent seismic network US from 2010 to 2020 (Figure 12). According to the distances from earthquakes to the array center (the geometric mean of station coordinates), we divide the 205 earthquakes into the near portion (with distances $<$ 10,000 km, 100 earthquakes) and far portion (with distances $>$ 11,500 km, 105 earthquakes). After similar processes as in the previous simulation experiment, we also extract several correlation signals resembling the core phases (Figure 13).

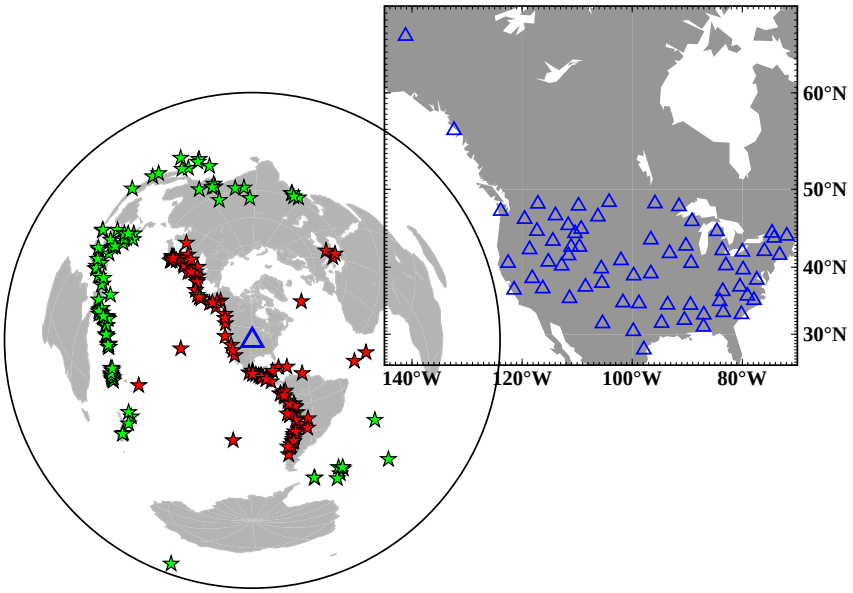

Figure 12. The distribution of large earthquakes (star) and stations in the US network (blue triangle). We divide the earthquakes into the near (red, with distances $< 10{,}000$ km) and far portion (with green, distances $> 11{,}500$ km). The upper right map zooms in the station distribution.

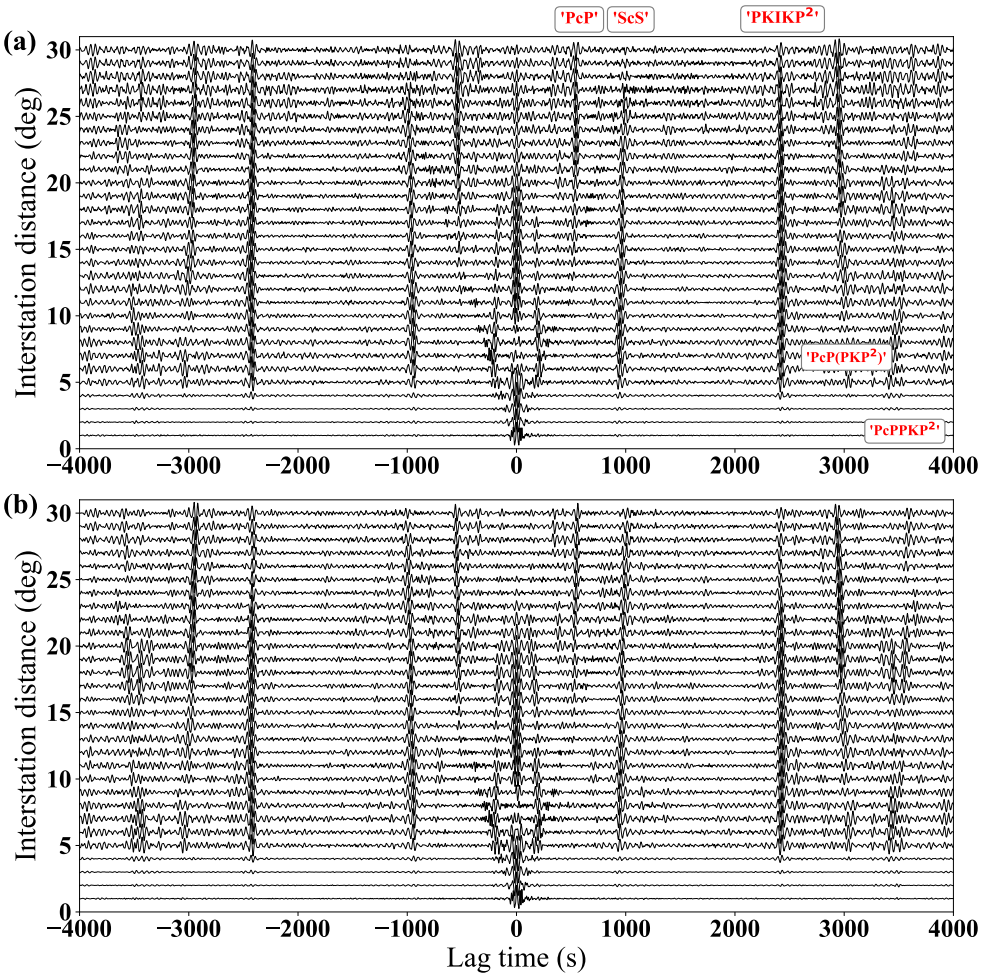

Figure 13. The normalized CCFs from earthquakes in the (a) near portion and (b) far portion. Some correlation signals resembling the Earth's deep reflections are labeled. The correlation signals are relatively weak in the inter-station distance from 1 ° to 4 ° due to normalizations with their peaks near the zero-lag times.

In the time window around the ScS arrivals, the correlation signals are not completely coincident from earthquakes in the near and far portion (Figure 14). It demonstrates that different event-receiver geometries indeed result in the emergence time variations of the correlation signals. Furthermore, the emergence time variations are also evident in the negative and positive lag time windows (Figure 15), which amounts to being caused by different earthquake distributions. The travel time shifts are quite small and are within 1/6 of the body wave correlation period, consistent with the theoretical prediction.

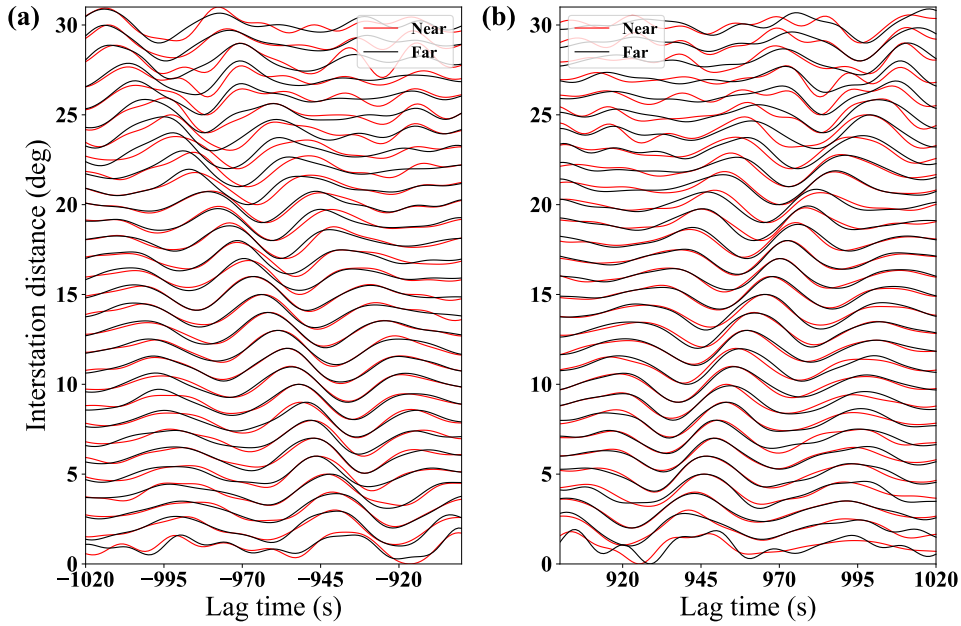

Figure 14. Comparisons between CCFs from near and far earthquakes in the *ScS* arrival time windows: (a) negative and (b) positive.

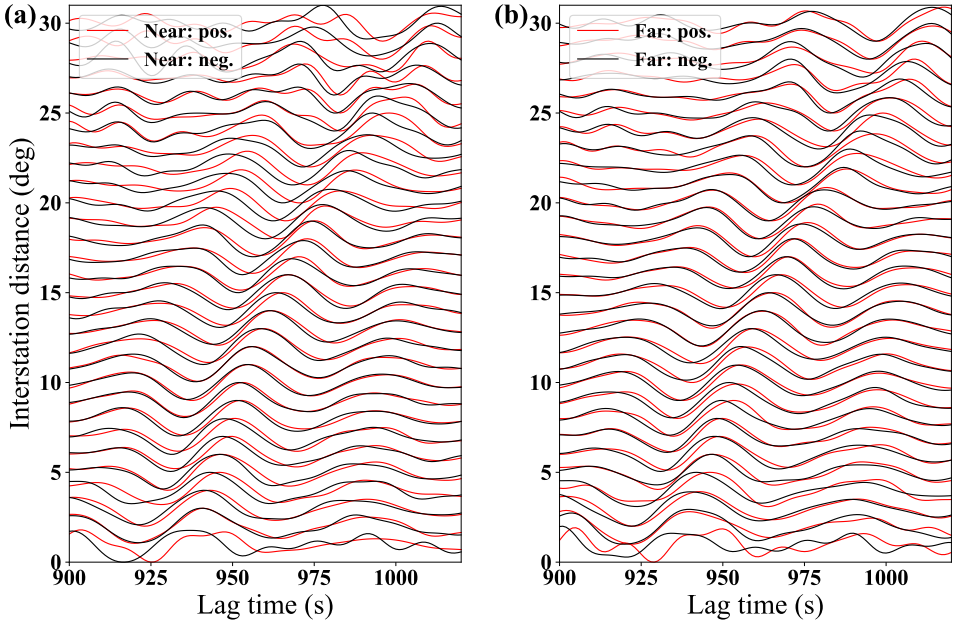

Figure 15. Comparisons between CCFs in the negative and positive *ScS* arrival time windows: (a) near portion and (b) far portion.

4 Discussion

Because the dispersion measurements of the correlation signals resemble those extracted from earthquake surface waves (e.g. Campillo & Paul, 2003; Shapiro & Campillo, 2004), the noise cross-correlation is now commonly recognized to recover impulse responses between two stations. Also, researchers have justified the relationship under controlled circumstances (e.g. Snieder, 2004; Sánchez-Sesma & Campillo, 2006; Boschi & Weemstra, 2015; Fichtner & Tsai, 2019). However, distinct features in coda correlations are not equivalent to Green's function of the propagation medium because the features resemble both the waves of Green's function and the exceptional spurious waves at the arrival time differences beteen the conventional deep reflections (Boué et al., 2014; Pham et al., 2018). Under the theoretical ray framework, we show that the correlations of coda waves with the same emitting slowness vector produce the two types of features. The result is similar to (Kennett & Pham, 2018). The dimension of the stationary phase zone is inversely proportional to the k-κ coefficient composed of the seismic wavenumber and the propagation distance of coda waves. In the late coda correlations, coda waves usually propagate for a long distance before arriving at two stations, which results in sufficiently small k-κ coefficients. Consequently, the coda correlations have a wide stationary phase zone, and earthquakes even far from the stationary points can, to some extent, contribute to constructive interferences. Indeed, becasue earthquakes are not always at the stationary points for the inter-station ray path, the correlation signals emerge earlier than the exact inter-station body waves.

The justification is under the geometric ray framework. Therefore, it is also applicable in other physics fields that allow geometric ray approximation, such as acoustics (Weaver & Lobkis, 2001) and electrokinetics (Duvall et al., 1993). Here, the theory can interpret the emergence of the correlation responses in Lobkis & Weaver (2001)'s ultrasonic laboratory test, which is somewhat a milestone of noise seismology. In Lobkis & Weaver (2001)'s test, the pulse generator on the specimen surface produces responses recorded by two transducers; and the correlation of coda responses produces correlation signals almost convergent to the propagating waves from one transducer to the other. Lobkis & Weaver (2001) attributed the test success to equipartitioned normal-mode energy produced by multiple reflections of acoustic waves in the specimen. However, the assumption may not be fully satisfied because in the test, the normal modes are more sensitive to the specimen surface. According to current results, the ultrasonic late coda correlations should correspond to sufficiently small k-κ coefficients. Thus, the pulse generator situates closely around the extended ray paths connecting two transducers, which produces the correlation signals that resemble the inter-transducer waves. Therefore, the current theory provides an alternative explanation for the emergence of "responses" in the ultrasonic laboratory test.

In late coda correlations, the current theory attributes the successful retrieval of "the inter-station body waves" to the sufficiently small k-κ coefficient. Exactly, when earthquakes situate on the great circle plane constrained by two stations and the coda wave propagates for a long distance, the k-κ interval is possibly smaller, and the correlation signals are more convergent to the inter-station waves for velocity. However, the current theory does not figure out how to retrieve the exact inter-station body waves. In realistic late coda correlations, it suggests that a time deviation up to 1/6 of the body wave correlation period may exist in the correlation signals. Geometric ray approximation and the stationary-phase analysis are high-frequency approximation methods that may bring bias into long-period coda correlations. Meanwhile, the geometric ray theory is invalid in some situations, e.g., there are caustics around the ray paths, reflections exceed the critical angles in discontinuous interfaces, or the noise sources are near-field. In these situations, this justification is inapplicable.

5 Conclusion

Based on geometric ray theory, we show that coda waves radiating with the same slowness vector can interfere constructively and produce the correlation signals at the travel time differences between coda waves on two seismic rays to two stations. Besides the distribution geometry of earthquakes, the correlation phase variations are also related to the dimension of the stationary phase zone which is inversely proportional to the k-κ coefficient composed of the seismic wavenumber and the propagation distance of the coda wave. The late seismic coda correlations usually correspond to sufficiently small k-κ coefficients, in the order of $10^{-4} \cdot km^{-1}$. Consequently, most of the large earthquakes situate in the stationary phase zone for the inter-station ray path and correlating codas from these earthquakes produces the correlation signals. However, the correlation signals may appear earlier than the exact inter-station body waves because earthquakes do not always situate at the stationary points. The synthetic and realistic coda correlations have validated the theoretical analysis. The theory is also applicable in other physics fields allowing for the geometric ray approximation. It can explain Lobkis & Weaver (2001)'s pioneering ultrasonic laboratory experiment. However, the theory is ineffective in complex media when geometric ray theory is inapplicable. This study demonstrates that in practical applications, the source-receiver geometry may result in an emergence time deviation up to 1/6 of the body wave correlation period. Thus, researchers should carefully investigate the impacts before using the reconstructed inter-station body waves in reliable seismic tomography.

Acknowledgments

This work was supported by the National Natural Science Foundation of China (Grants 41790465 and U1901602), Shenzhen Offshore Oil and Gas Exploration Technology (Grant ZDSYS20190902093007855).

The facilities of Incorporated Research Institutions for Seismology (IRIS) Data Services, especially the IRIS Data Management Center gave us access to real waveforms. IRIS Data Services are funded through the Seismological Facilities for the Advancement of Geoscience (SAGE) Award of the National Science Foundation under Cooperative Support Agreement EAR-1851048. Data were made freely available from the US national seismic network facility and downloaded via Obspy (Krischer et al., 2015). We are also thankful to Nozomu Takeuchi for providing the DSM software (http://www.eri.u-tokyo.ac.jp/people/takeuchi/software). Some figures are created using Generic Mapping Tools (Wessel & Smith, 1998).

References

Bensen, G. D., Ritzwoller, M. H., Barmin, M. P., Levshin, A. L., Lin, F., Moschetti, M. P., … Yang, Y. (2007). Processing seismic ambient noise data to obtain reliable broad-band surface wave dispersion measurements. *Geophysical Journal International*, *169*(3), 1239-1260.

Boschi, L., & Weemstra, C. (2015). Stationary-phase integrals in the cross correlation of ambient noise. *Reviews of Geophysics*, *53*(2), 411-451. doi: 10.1002/2014RG000455

Boué, P., Poli, P., Campillo, M., & Roux, P. (2014). Reverberations, coda waves and ambient noise: Correlations at the global scale and retrieval of the deep phases. *Earth & Planetary ence Letters*, *391*, 137-145.

Campillo, M., & Paul, A. (2003). Long-range correlations in the diffuse seismic coda. *Science*, *299*(5606), 547–549.

Chapman, C. (2004). *Fundamentals of seismic wave propagation.* Cambridge University Press.

Duvall, T. L., Jeffferies, S., Harvey, J., & Pomerantz, M. (1993). Time–distance helioseismology. *Nature*, *362*(6419), 430–432.

Fichtner, A., Stehly, L., Ermert, L., & Boehm, C. (2016). Generalized interferometry –I: theory for interstation correlations. *Geophysical Journal International*, *208*(2), 603-638. doi: 10.1093/gji/ggw420

Fichtner, A., & Tsai, V. C. (2019). Theoretical foundations of noise interferometry. In (p. 109-143). Cambridge University Press, Cambridge, UK. doi: 10.1017/9781108264808.006

Froment, B., Campillo, M., Roux, P., Gouédard, P., Verdel, A., & Weaver, R. L. (2010).

Estimation of the effect of nonisotropically distributed energy on the apparent arrival time in correlations. *Geophysics*, *75*(5), SA85-SA93. doi: 10.1190/1.3483102

Huang, H.-H., Lin, F.-C., Tsai, V. C., & Koper, K. D. (2015). High-resolution probing of inner core structure with seismic interferometry. *Geophysical Research Letters*, *42*(24), 10,622-10,630. doi: 10.1002/2015GL066390

Kawai, K., Takeuchi, N., & Geller, R. J. (2006). Complete synthetic seismograms up to 2 hz for transversely isotropic spherically symmetric media. *Geophysical Journal International*, *164*(2), 411-424. doi: 10.1111/j.1365-246X.2005.02829.x

Kennett, B., & Engdahl, E. R. (1991). Traveltimes for global earthquake location and phase identification. *Geophysical Journal International*, *105*(2), 429-465. doi: 10.1111/j.1365-246X.1991.tb06724.x

Kennett, B., & Pham, T.-S. (2018). The nature of Earth's correlation wavefield: late coda of large earthquakes. *Proceedings of the Royal Society A: Mathematical, Physical and Engineering Sciences*, *474*, 20180082. Retrieved from `https://royalsocietypublishing.org/doi/abs/10.1098/rspa.2018.0082` doi: 10.1098/rspa.2018.0082

Krischer, L., Megies, T., Barsch, R., Beyreuther, M., Lecocq, T., Caudron, C., & Wassermann, J. (2015). Obspy : a bridge for seismology into the scientific python ecosystem. *COMPUTATIONAL SCIENCE & DISCOVERY*, *8*(1), 17.

Li, L., Boué, P., & Campillo, M. (2020). Observation and explanation of spurious seismic signals emerging in teleseismic noise correlations. *Solid Earth*, *11*, 173-184. doi: 10.5194/se-11-173-2020

Lin, F.-C., & Tsai, V. C. (2013). Seismic interferometry with antipodal station pairs. *Geophysical Research Letters*, *40*(17), 4609–4613.

Lin, F.-C., Tsai, V. C., Schmandt, B., Duputel, Z., & Zhan, Z. (2013). Extracting seismic core phases with array interferometry. *Geophysical Research Letters*, *40*(6), 1049-1053.

Liu, T., & Zhang, H. (2018). Asymptotic analysis for dispersion relations and travel times in noise cross-correlations: spherically symmetric case. *Proceedings of The Royal Society A Mathematical Physical and Engineering ences*, *474*(2218).

Lobkis, O. I., & Weaver, R. L. (2001). On the emergence of the green's function in the correlations of a diffuse field. *The Journal of the Acoustical Society of America*, *110*(6), 3011-3017. Retrieved from `https://doi.org/10.1121/1.1417528` doi: 10.1121/1.1417528

Pham, T.-S., Tkalčić, H., Sambridge, M., & Kennett, B. (2018). Earth's correlation wavefield: Late coda correlation. *Geophysical Research Letters*, *45*(7), 3035-3042. doi: 10.1002/2018GL077244

Poli, P., Campillo, M., & Pedersen, H. (2012). Body-wave imaging of Earth's mantle discontinuities from ambient seismic noise. *Science*, *338*(6110), 1063 - 1065.

Poli, P., Thomas, C., Campillo, M., & Pedersen, H. A. (2015). Imaging the D" reflector with noise correlations. *Geophysical Research Letters*, *42*(1), 60-65.

Roux, P., Sabra, K. G., Geostoft, P., & Kuperman, W. A. (2005). P-waves from cross-correlation of seismic noise. *Geophysical Research Letters*, *32*(19), 312-321.

Sager, K., Boehm, C., Ermert, L., Krischer, L., & Fichtner, A. (2018). Sensitivity of seismic noise correlation functions to global noise sources. *Journal of Geophysical Research: Solid Earth*, *123*(8), 6911-6921. doi: 10.1029/2018JB016042

Sánchez-Sesma, F. J., & Campillo, M. (2006). Retrieval of the Green's Function from Cross Correlation: The Canonical Elastic Problem. *Bulletin of the Seismological Society of America*, *96*(3), 1182-1191. doi: 10.1785/0120050181

Sens-Schönfelder, C., Snieder, R., & Stähler, S. C. (2015). The lack of equipartitioning in global body wave coda. *Geophysical Research Letters*, *42*(18), 7483-7489. doi: 10.1002/2015GL065108

Shapiro, N. M., & Campillo, M. (2004). Emergence of broadband Rayleigh waves from correlations of the ambient seismic noise. *Geophysical Research Letters*, *31*(31), 07614.

Snieder, R. (2004). Extracting the Green's function from the correlation of coda waves: a derivation based on stationary phase. *Physical Review E Statistical Nonlinear & Soft Matter Physics*, *69*(2), 046610.

Tanimoto, T. (2008). Normal-mode solution for the seismic noise cross-correlation method. *Geophysical Journal International*, *175*(3), 1169-1175.

Tatiana, Y., Tatiana, K., & Eugenia, L. (2016). Effect of earthquakes on ambient noise surface wave tomography in upper-mantle studies. *Geophysical Journal International*, *205*, 1208-1220.

Tkalčić, H., & Pham, T.-S. (2018). Shear properties of Earth's inner core constrained by a detection of J waves in global correlation wavefield. *science*, *362*(6412), 329-332.

Tonegawa, T., Nishida, K., Watanabe, T., & Shiomi, K. (2009). Seismic interferometry of teleseicmic S-wave coda for retrieval of body waves: An application to the Philippine Sea slab underneath the Japanese Islands. *Geophysical Journal International*, *178*(3), 1574-1586. doi: 10.1111/j.1365-246X.2009.04249.x

Tromp, J., Luo, Y., Hanasoge, S., & Peter, D. (2010). Noise cross-correlation sensitivity kernels. *Geophysical Journal International*, *183*(2), 791-819. doi: 10.1111/j.1365-246X.2010.04721.x

Tsai, V. C. (2009). On establishing the accuracy of noise tomography travel-time measurements in a realistic medium. *Geophysical Journal International*, *178*(3), 1555-1564. doi: 10.1111/j.1365-246X.2009.04239.x

Wang, S., & Tkalčić, H. (2020). Seismic event coda-correlation: Toward global

coda-correlation tomography. *Journal of Geophysical Research: Solid Earth*, *125*(4), e2019JB018848. (e2019JB018848 2019JB018848) doi: 10.1029/2019JB018848

Wapenaar, K. (2004). Retrieving the elastodynamic Green's function of an arbitrary inhomogeneous medium by cross correlation. *Physical Review Letters*, *93*(25), 254301.

Wapenaar, K., & Fokkema, J. (2006). Green's unction representations for seismic interferometry. *Geophysics*, *71*(4), SI33-SI46. doi: 10.1190/1.2213955

Weaver, R. L., & Lobkis, O. I. (2001). Ultrasonics without a source: thermal fluctuation correlations at MHz frequencies. *Physical Review Letters*, *87*(13), 134301.

Wessel, P., & Smith, W. H. F. (1998). New, improved version of generic mapping tools released. *Eos, Transactions American Geophysical Union*, *79*(47), 579-579. doi: 10.1029/98EO00426

Wu, B., Xia, H. H., Wang, T., & Shi, X. (2018). Simulation of core phases from coda interferometry. *Journal of Geophysical Research: Solid Earth*, *123*(6), 4983-4999. doi: 10.1029/2017JB015405

Yao, H., & van der Hilst, R. D. (2009). Analysis of ambient noise energy distribution and phase velocity bias in ambient noise tomography, with application to SE Tibet. *Geophysical Journal International*, *179*(2), 1113-1132.

Zhan, Z., Ni, S., Helmberger, D. V., & Clayton, R. W. (2010). Retrieval of Moho-reflected shear wave arrivals from ambient seismic noise. *Geophysical Journal International*, *182*(1), 408-420. doi: 10.1111/j.1365-246X.2010.04625.x

Appendix A Eigenvalue Decomposition of the Hessian Matrix

The Hessian matrix $\boldsymbol{H}_{mn}(\boldsymbol{x}_s)$ is diagonalizable with real eigenvalues and eigenvectors as

$$\boldsymbol{H}_{mn}(\omega, \boldsymbol{x}_s) = \boldsymbol{E}_{mn}^T(\boldsymbol{x}_s)\boldsymbol{\Lambda}_{mn}(\boldsymbol{x}_s)\boldsymbol{E}_{mn}(\boldsymbol{x}_s) \ ,$$

where $\boldsymbol{E}(\boldsymbol{x}_s)$ represents the coordinate transformation matrix, with $\det[\boldsymbol{E}_{mn}(\boldsymbol{x}_s)] = 1$. We represent the diagonal matrix $\boldsymbol{\Lambda}_{mn}(\boldsymbol{x}_s)$ as

$$\boldsymbol{\Lambda}_{mn}(\boldsymbol{x}_s) = \mathrm{diag}[\nu_1^{(mn)}(\boldsymbol{x}_s), \nu_2^{(mn)}(\boldsymbol{x}_s), \nu_3^{(mn)}(\boldsymbol{x}_s)] \ .$$

Here, we prove that

(i) $\boldsymbol{E}_{mn} = [\hat{\boldsymbol{\eta}}_1(\boldsymbol{x}_s), \hat{\boldsymbol{\eta}}_2(\boldsymbol{x}_s), \hat{\boldsymbol{\eta}}_3]$, with $\hat{\boldsymbol{\eta}}_3$ along $\mathcal{L}_m(\boldsymbol{x}_s)$ in the source region. $\hat{\boldsymbol{\eta}}_1(\boldsymbol{x}_s)$ and $\hat{\boldsymbol{\eta}}_2(\boldsymbol{x}_s)$ correspond to the steepest and slowness descent direction of the distance difference at $\boldsymbol{x}_s$, where the distances are from Π_m and Π'_n to the common tangent plane of the two wavefronts, respectively.

(ii) $\hat{\boldsymbol{\eta}}_1$ and $\hat{\boldsymbol{\eta}}_2$ correspond to the SH and SV direction in a radially homogeneous medium.

(iii) $\mathbf{\Lambda}_{mn}(\boldsymbol{x}_s)$ is

$$\begin{aligned}\mathbf{\Lambda}_{mn}(\boldsymbol{x}_s) =& \text{diag}[\nu_1^{(mn)}(\boldsymbol{x}_s), \nu_2^{(mn)}(\boldsymbol{x}_s), \nu_3^{(mn)}(\boldsymbol{x}_s)] \\ =& \frac{1}{c}\begin{bmatrix} \kappa_1(\boldsymbol{x}_s, \mathcal{L}'_n) - \kappa_1(\boldsymbol{x}_s, \mathcal{L}_m) & 0 & 0 \\ 0 & \kappa_2(\boldsymbol{x}_s, \mathcal{L}'_n) - \kappa_2(\boldsymbol{x}_s, \mathcal{L}_m) & 0 \\ 0 & 0 & 0 \end{bmatrix} ,\end{aligned}$$

with the velocity $c = \alpha$ or β. $\kappa_1(\boldsymbol{x}_s, \mathcal{L}_m)$ and $\kappa_1(\boldsymbol{x}_s, \mathcal{L}'_n)$ represent the curvature of curves at $\boldsymbol{x}_s$ in the η_1 direction on Π_m and Π'_n, respectively. $\kappa_2(\boldsymbol{x}_s, \mathcal{L}_m)$ and $\kappa_2(\boldsymbol{x}_s, \mathcal{L}'_n)$ are the same except in the η_2 direction.

Proof:

(i) In the homogeneous source region, we establish the Frenet frame as $\{\boldsymbol{x}_s; \hat{\boldsymbol{\eta}}_1, \hat{\boldsymbol{\eta}}_2, \hat{\boldsymbol{\eta}}_3\}$, with the unit vector $\hat{\boldsymbol{\eta}}_3$ along the ray, and the two orthogonal unit vectors $\hat{\boldsymbol{\eta}}_1(\boldsymbol{x}_s)$ and $\hat{\boldsymbol{\eta}}_2(\boldsymbol{x}_s)$ perpendicular to $\hat{\boldsymbol{\eta}}_3$. $\hat{\boldsymbol{\eta}}_3$ is irrelevant to $\boldsymbol{x}_s$ because $\mathcal{L}_m$ is straight in V. At any $\boldsymbol{x}_s$ along the ray, as in Eq. (7), it satisfies

$$\nabla\psi_{mn}(\boldsymbol{x})|_{\boldsymbol{x}=\boldsymbol{x}_s} = 0 \ . \tag{A1}$$

We obtain

$$\frac{\partial^2\psi_{mn}(\boldsymbol{x})}{\partial\eta_i\partial\eta_3}|_{\boldsymbol{x}=\boldsymbol{x}_s} = 0 \ , \tag{A2}$$

with $i = 1, 2, 3$. It means that $\hat{\boldsymbol{\eta}}_3$ is a eigenvector in $\boldsymbol{E}_{mn}(\boldsymbol{x}_s)$, and the corresponding eigen value

$$\nu_3^{(mn)}(\boldsymbol{x}_s) = 0 \ . \tag{A3}$$

Now we determine the other two eigen vectors. We represent Π_m as $\eta_3 = \phi_m(\eta_1, \eta_2)$. The unit normal vector of Π_m is

$$\hat{\boldsymbol{n}} = \frac{1}{\sqrt{(\partial\phi_m/\partial\eta_1)^2 + (\partial\phi_m/\partial\eta_2)^2 + 1}}(\frac{\partial\phi_m}{\partial\eta_1}, \frac{\partial\phi_m}{\partial\eta_2}, -1) \ . \tag{A4}$$

For a point (ξ_1, ξ_2) in the tangent plane, the travel time function $T(\xi_1, \xi_2; \boldsymbol{x}_a, \mathcal{L}_m)$ is

$$\begin{aligned}T(\xi_1, \xi_2; \boldsymbol{x}_a, \mathcal{L}_m) =& -\frac{\phi_m}{c\hat{\boldsymbol{n}}\cdot\hat{\boldsymbol{\eta}}_3} \\ =& \frac{\phi_m}{c}\sqrt{(\partial\phi_m/\partial\eta_1)^2 + (\partial\phi_m/\partial\eta_2)^2 + 1} \ .\end{aligned} \tag{A5}$$

The point (ξ_1, ξ_2) is projected by (η_1, η_2) along $\mathcal{L}_m$ as (Figure A1)

$$\begin{aligned}\xi_1 &= \eta_1 + \phi_m\frac{\partial\phi_m}{\partial\eta_1} \\ \xi_2 &= \eta_2 + \phi_m\frac{\partial\phi_m}{\partial\eta_2}\end{aligned} \ . \tag{A6}$$

Noting that

$$\phi_m(0,0) = 0, \quad \frac{\partial\phi_m}{\partial\eta_1}(0,0) = 0 \quad \text{and} \quad \frac{\partial\phi_m}{\partial\eta_2}(0,0) = 0 \ , \tag{A7}$$

we obtain

$$\begin{bmatrix} \frac{\partial \xi_1}{\partial \eta_1} & \frac{\partial \xi_1}{\partial \eta_2} \\ \frac{\partial \xi_2}{\partial \eta_1} & \frac{\partial \xi_2}{\partial \eta_2} \end{bmatrix} |_{(0,0)} = \begin{bmatrix} 1 & 0 \\ 0 & 1 \end{bmatrix} . \tag{A8}$$

Based on the chain rule, we have

$$\begin{aligned} c\frac{\partial T}{\partial \xi_1}(0,0;\boldsymbol{x}_a,\mathcal{L}_m) =& \frac{\partial \phi_m}{\partial \eta_1}(0,0) \\ c\frac{\partial T}{\partial \xi_2}(0,0;\boldsymbol{x}_a,\mathcal{L}_m) =& \frac{\partial \phi_m}{\partial \eta_2}(0,0) \end{aligned} , \tag{A9}$$

and

$$\begin{aligned} c\frac{\partial^2 T}{\partial \xi_1^2}(0,0;\boldsymbol{x}_a,\mathcal{L}_m) =& \frac{\partial^2 \phi_m}{\partial \eta_1^2}(0,0) \\ c\frac{\partial^2 T}{\partial \xi_2^2}(0,0;\boldsymbol{x}_a,\mathcal{L}_m) =& \frac{\partial^2 \phi_m}{\partial \eta_2^2}(0,0) \\ c\frac{\partial^2 T}{\partial \xi_1 \xi_2}(0,0;\boldsymbol{x}_a,\mathcal{L}_m) =& \frac{\partial^2 \phi_m}{\partial \eta_1 \eta_2}(0,0) \end{aligned} , \tag{A10}$$

At the same $\boldsymbol{x}_s$, we can represent Π_n' as $\eta_3 = \phi_n'(\eta_1, \eta_2)$, and obtain similar results. Let that

$$\chi_{mn}(\eta_1, \eta_2) = \phi_n'(\eta_1, \eta_2) - \phi_m(\eta_1, \eta_2) , \tag{A11}$$

which represents the difference between the distances from Π_m and Π_n' to the common tangent plane of the two wavefronts. We have

$$\begin{aligned} \nabla \psi_{mn}(\boldsymbol{x}_s) =& \frac{1}{c} \nabla \chi(0,0) = 0 \\ \boldsymbol{H}_{mn}(\boldsymbol{x}_s) =& \frac{1}{c} \nabla \nabla \chi(0,0) . \end{aligned} \tag{A12}$$

In the $\eta_1 \eta_2$ plane, we represent a small circle around $\boldsymbol{x}_s$ as

$$\boldsymbol{r} = \boldsymbol{x}_s + \epsilon(\cos\theta \hat{\boldsymbol{\eta}}_1 + \sin\theta \hat{\boldsymbol{\eta}}_2) , \tag{A13}$$

where the angle θ is between $\boldsymbol{r}$ and $\hat{\boldsymbol{\eta}}_1$. At $\boldsymbol{x}_s$, $\chi_{mn}(\boldsymbol{r})$ can be expanded by Taylor series as

$$\begin{aligned} \chi_{mn}(\boldsymbol{r}) =& \epsilon^2(\cos^2\theta \frac{\partial^2 \chi}{\partial \eta_1^2} + \sin^2\theta \frac{\partial^2 \chi}{\partial \eta_2^2})|(0,0) + \mathcal{O}(\epsilon^4) \\ =& \epsilon^2[\frac{\partial^2 \chi}{\partial \eta_1^2} + \sin^2\theta(\frac{\partial^2 \chi}{\partial \eta_2^2} - \frac{\partial^2 \chi}{\partial \eta_1^2})]|(0,0) + \mathcal{O}(\epsilon^4) \end{aligned} . \tag{A14}$$

$\chi_{mn}(\boldsymbol{r})$ has two extreme values at $\theta = 0$ and $\theta = \pi/2$. Thus, $\hat{\boldsymbol{\eta}}_1$ and $\hat{\boldsymbol{\eta}}_2$ correspond to the steepest and slowest descent direction of $\chi_{mn}(\eta_1, \eta_2)$ at $\boldsymbol{x}_s$, respectively.

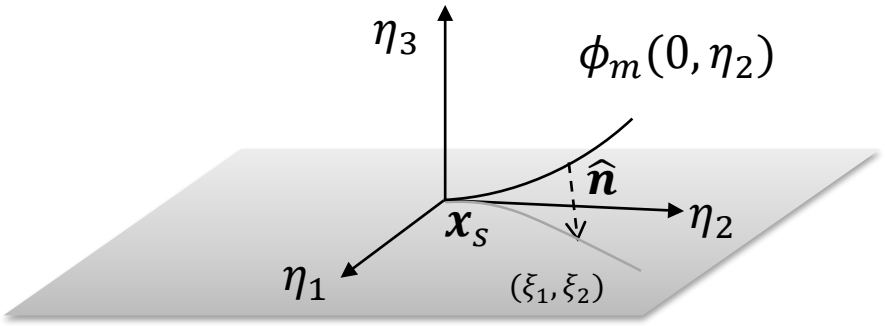

Figure A1. Ray propagation from Π_m to the tangent $\eta_1\eta_2$ plane within V.

(ii) In V, at any $\eta_1\eta_2$ plane with respect to $\boldsymbol{x}_s + h\hat{\boldsymbol{\eta}}_3$, where h represents the distance to the tangent plane at $\boldsymbol{x}_s$ (Figure A2), the point (ξ_1, ξ_2) is projected by (η_1, η_2) along $\mathcal{L}_m$ as

$$\begin{aligned} \xi_1 &= \eta_1 + (\phi_m + h)\frac{\partial \phi_m}{\partial \eta_1} \\ \xi_2 &= \eta_2 + (\phi_m + h)\frac{\partial \phi_m}{\partial \eta_2} \end{aligned} , \tag{A15}$$

We obtain

$$\frac{\partial \xi_1}{\partial \eta_1}(0,0) = 1, \quad \frac{\partial \xi_2}{\partial \eta_2}(0,0) = 1, \quad \frac{\partial \xi_1}{\partial \eta_2}(0,0) = \frac{\partial \xi_2}{\partial \eta_1}(0,0) = h\frac{\partial^2 \phi_m}{\partial \eta_1 \partial \eta_2}(0,0) \ . \tag{A16}$$

Therefore, for any curve on Π_m passing through $\boldsymbol{x}_s$, to ensure that the projection direction are the same at the point, it requires

$$\frac{\partial^2 \phi_m}{\partial \eta_1 \partial \eta_2}(0,0) = 0 \ . \tag{A17}$$

For the curve on Π_n', it similarly requires

$$\frac{\partial^2 \phi_n'}{\partial \eta_1 \partial \eta_2}(0,0) = 0 \ . \tag{A18}$$

The condition is usually invalid when the medium outside the source region is inhomogeneous, so $\hat{\boldsymbol{\eta}}_1$ and $\hat{\boldsymbol{\eta}}_2$ vary at different $\boldsymbol{x}_s$.

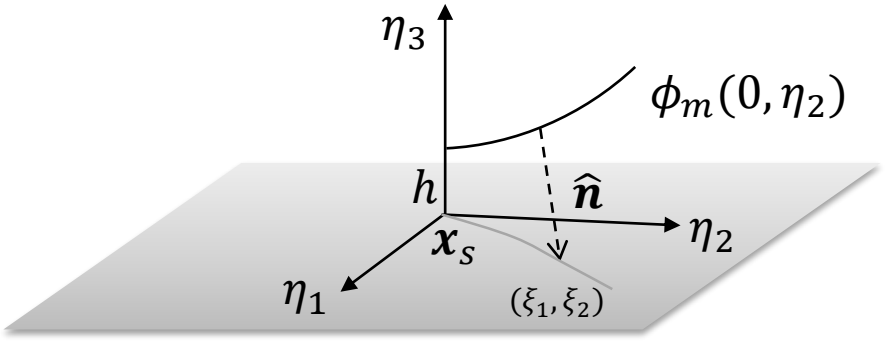

Figure A2. Ray propagation from Π_m to the $\eta_1\eta_2$ plane with a distance of h to the tangent $\eta_1\eta_2$ plane.

Specially, in a laterally or radially homogeneous medium, Π_m and Π'_n are cylindrically symmetric. Let $\hat{\boldsymbol{\eta}}_1$ and $\hat{\boldsymbol{\eta}}_2$ in the SV and SH direction. According to symmetry, we can obtain

$$\frac{\partial^2\phi_m}{\partial\eta_1\partial\eta_2}(0,0)=0, \quad \text{and} \quad \frac{\partial^2\phi'_n}{\partial\eta_1\partial\eta_2}(0,0)=0\ , \tag{A19}$$

and moreover,

$$\frac{\partial\chi^2_{mn}}{\partial\eta_1\partial\eta_2}(0,0)=0\ . \tag{A20}$$

Therefore, the two eigenvectors $\hat{\boldsymbol{\eta}}_1$ and $\hat{\boldsymbol{\eta}}_2$ are at the SV and SH direction. They are certainly constant in the laterally or radially homogeneous medium.

(iii) In the $\eta_1\eta_3$ plane, the two curves on Π_m and Π'_n are $(\eta_1,\phi_m(\eta_1,0))$ and $(\eta_1,\phi'_n(\eta_1,0))$, respectively. For the two curves at $\boldsymbol{x}_s$, by definition (in the situation that $\hat{\boldsymbol{\eta}}_3$ points to the curve direction), we obtain the curvature

$$\begin{aligned}\kappa_1(\boldsymbol{x}_s,\mathcal{L}_m)&=\frac{\partial^2\phi_m/\partial\eta_1^2}{\sqrt{[(1+(\partial\phi_m/\partial\eta_1)^2]^3}}(0,0)=\frac{\partial^2\phi_m}{\partial\eta_1^2}(0,0)\\ \kappa_1(\boldsymbol{x}_s,\mathcal{L}'_n)&=\frac{\partial^2\phi'_n/\partial\eta_1^2}{\sqrt{[(1+(\partial\phi'_n/\partial\eta_1)^2]^3}}(0,0)=\frac{\partial^2\phi'_n}{\partial\eta_1^2}(0,0)\end{aligned}\ , \tag{A21}$$

Similarly, for Π_m and Π'_n in the $\eta_2\eta_3$ plane, we have

$$\begin{aligned}\kappa_2(\boldsymbol{x}_s,\mathcal{L}_m)&=\frac{\partial^2\phi_m}{\partial\eta_2^2}(0,0)\\ \kappa_2(\boldsymbol{x}_s,\mathcal{L}'_n)&=\frac{\partial^2\phi'_n}{\partial\eta_2^2}(0,0)\end{aligned}\ . \tag{A22}$$

Finally, there is

$$\begin{aligned}\boldsymbol{\Lambda}_{mn}(\boldsymbol{x}_s) =& \frac{1}{c}\begin{bmatrix} \partial^2\chi_{mn}/\partial\eta_1^2(0,0) & 0 & 0 \\ 0 & \partial^2\chi_{mn}/\partial\eta_2^2(0,0) & 0 \\ 0 & 0 & 0 \end{bmatrix} \\ =& \frac{1}{c}\begin{bmatrix} \kappa_1(\boldsymbol{x}_s,\mathcal{L}'_n)-\kappa_1(\boldsymbol{x}_s,\mathcal{L}_m) & 0 & 0 \\ 0 & \kappa_2(\boldsymbol{x}_s,\mathcal{L}'_n)-\kappa_2(\boldsymbol{x}_s,\mathcal{L}_m) & 0 \\ 0 & 0 & 0 \end{bmatrix} .\end{aligned} \tag{A23}$$

This is the desired result.

Appendix B The Sign of the Eigenvalues

We investigate the sign of $\nu_1^{(mn)}(\boldsymbol{x}_s)$ and $\nu_2^{(mn)}(\boldsymbol{x}_s)$ when $\mathcal{L}_m$ and $\mathcal{L}'_n$ coincide. At any $\boldsymbol{x}_s$, still, we build the Frenet frame as $\{\boldsymbol{x}_s;\hat{\boldsymbol{\eta}}_1,\hat{\boldsymbol{\eta}}_2,\hat{\boldsymbol{\eta}}_3\}$, and represent Π_m and Π'_n as $\eta_3=\phi_m(\eta_1,\eta_2)$ and $\eta_3=\phi'_n(\eta_1,\eta_2)$, respectively. At a noise source $\boldsymbol{x}_s+\epsilon\hat{\boldsymbol{r}}$ on Π_m in V_- (Figure B1), based on Fermat's principle, there should be

$$\delta T(\boldsymbol{x}_b,\boldsymbol{x}_s+\epsilon\hat{\boldsymbol{r}},\mathcal{L}'_n)=0 , \tag{B1}$$

with $\hat{\boldsymbol{r}}$ denoting a unit vector and δ denoting the variation. In the $\eta_1\eta_3$ coordinate system, because Π_m is convex, it is easy to prove that $T(\boldsymbol{x}_b,\boldsymbol{x}_s+\epsilon\hat{\boldsymbol{r}},\mathcal{L}'_n)$ corresponds to the minimum travel time in the path variation of $\mathcal{L}'_n$. Then, we have

$$T(\boldsymbol{x}_b,\boldsymbol{x}_s+\epsilon\hat{\boldsymbol{r}},\mathcal{L}'_n)<T(\boldsymbol{x}_b,\boldsymbol{x}_a,\mathcal{L}'_n)+T(\boldsymbol{x}_a,\boldsymbol{x}_s+\epsilon\hat{\boldsymbol{r}},\mathcal{L}_m)=T(\boldsymbol{x}_b,\boldsymbol{x}_s,\mathcal{L}'_n) . \tag{B2}$$

This inequality means that the seismic wave along $\mathcal{L}'_n$ first arrive Π_m and then Π'_n, as shown in Figure B1. We have

$$\chi_{mn}(\eta_1,\eta_2)=\phi'_n(\eta_1,\eta_2)-\phi_m(\eta_1,\eta_2)<0 . \tag{B3}$$

Because at the stationary point $\boldsymbol{x}_s$, $\chi_{mn}(0,0)=0$ which is the maximum value, based on the extreme value theorem,

$$\frac{\partial^2\chi_{mn}}{\partial\eta_1^2}<0 \quad \text{and} \quad \frac{\partial^2\chi_{mn}}{\partial\eta_2^2}<0 , \tag{B4}$$

i.e.

$$\nu_1^{(mn)}(\boldsymbol{x}_s)<0 \quad \text{and} \quad \nu_2^{(mn)}(\boldsymbol{x}_s)<0 . \tag{B5}$$

Similarly, in V_+, we can prove

$$\nu_1^{(mn)}(\boldsymbol{x}_s)>0 \quad \text{and} \quad \nu_2^{(mn)}(\boldsymbol{x}_s)>0 . \tag{B6}$$

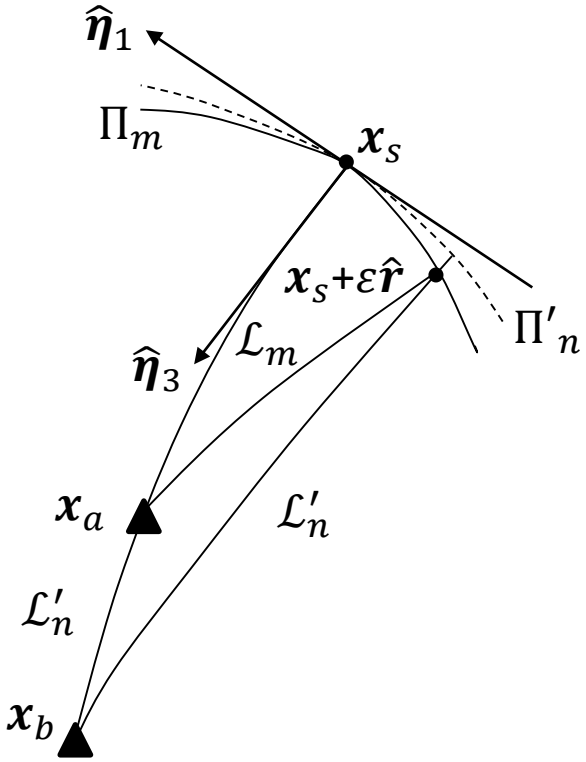

Figure B1. (a) The comparison of travel time $T(\boldsymbol{x}_b, \boldsymbol{x}_s, \mathcal{L}'_n)$ and $T(\boldsymbol{x}_b, \boldsymbol{x}_s + \epsilon\hat{\boldsymbol{r}}, \mathcal{L}'_n)$, with $\boldsymbol{x}_s$ and $\boldsymbol{x}_s + \epsilon\hat{\boldsymbol{r}}$ on Π_m.